

**Influence of El Niño on atmospheric CO<sub>2</sub> over the tropical Pacific Ocean:  
findings from NASA's OCO-2 mission**

A. Chatterjee<sup>1,2\*</sup>, M. M. Gierach<sup>3</sup>, A. J. Sutton<sup>4,5</sup>, R. A. Feely<sup>4</sup>, D. Crisp<sup>3</sup>, A. Eldering<sup>3</sup>, M. R.  
Gunson<sup>3</sup>, C. W. O'Dell<sup>6</sup>, B. B. Stephens<sup>7</sup>, D. S. Schimel<sup>3</sup>

<sup>1</sup> Universities Space Research Association, Columbia, MD

<sup>2</sup> NASA Global Modeling and Assimilation Office, Greenbelt, MD

<sup>3</sup> Jet Propulsion Laboratory, California Institute of Technology, Pasadena, CA

<sup>4</sup> NOAA Pacific Marine Environmental Laboratory, Seattle, WA

<sup>5</sup> Joint Institute for the Study of the Atmosphere and Ocean, University of Washington, Seattle,  
WA

<sup>6</sup> Colorado State University, Fort Collins, CO

<sup>7</sup> National Center for Atmospheric Research, Boulder, CO

\*Correspondence to: abhishek.chatterjee@nasa.gov

1   **Abstract:**

2   Space-borne observations of CO<sub>2</sub> from the Orbiting Carbon Observatory-2 are used to  
3   characterize the response of the tropical atmospheric CO<sub>2</sub> concentrations to the strong El Niño  
4   event of 2015-2016. Correlations between atmospheric CO<sub>2</sub> growth rate and the El Niño  
5   Southern Oscillation have been well known; however, the magnitude of the correlation and the  
6   timing of the responses of oceanic and terrestrial carbon cycle remain poorly constrained in  
7   space and time. Here we use space-based CO<sub>2</sub> observations to confirm that the tropical Pacific  
8   Ocean does play an early and important role in modulating the changes in atmospheric CO<sub>2</sub>  
9   concentrations during El Niño events – phenomenon inferred but not previously observed due to  
10   lack of high-density, broad-scale CO<sub>2</sub> observations over the Tropics.

11

12   **One Sentence Summary:**

13   NASA's OCO-2 mission provides a first-hand look at the space-time evolution of tropical  
14   atmospheric CO<sub>2</sub> concentrations in response to the 2015-2016 El Niño

## **Main Text:**

El Niño Southern Oscillation, or ENSO, is the dominant mode of tropical climate variability on interannual to decadal timescales (1-5) and is correlated with large inter-annual variability in global atmospheric CO<sub>2</sub> concentrations (6-19). Studying the response of the carbon cycle to this natural climate phenomenon is critical to understand and quantify the sensitivity of the carbon cycle to climate variability, and by extension to climate generally (20). Although the ENSO cycle originates in the equatorial Pacific, its impact on the carbon cycle is felt globally due to its regional teleconnections (22-23) and influences on atmospheric and ocean circulation, precipitation, temperature, and fire emissions (1, 24-26). Partitioning the response of the constituent components of the carbon cycle to a complete El Niño event has been challenging because of the limited number of CO<sub>2</sub> observations over the tropical land and ocean regions.

Observations of atmospheric CO<sub>2</sub> from space provide a global view of the carbon cycle that can be used to describe phenomena that have been previously pieced together from sparse *in situ* data. NASA's Orbiting Carbon Observatory-2 (OCO-2) mission was successfully launched on July 2, 2014 and started providing science data in early September 2014 (70). Within the first two years of operation of the OCO-2 mission, a major El Niño (warm phase of the ENSO) occurred (27-30). We provide an approach for studying the temporal sequence of El Niño-induced changes in global CO<sub>2</sub> concentrations using observations from the OCO-2 mission that are validated with the Tropical Atmosphere Ocean (TAO) mooring CO<sub>2</sub> data. We see a response from the tropical Pacific Ocean during the early stages of an El Niño event and a lagged (and much larger) terrestrial signal as the El Niño reaches maturity.

## ***El Niño and the global carbon cycle***

Correlations between the atmospheric CO<sub>2</sub> growth rate and El Niño activity have been reported since the 1970s (6-8, 31-32), although the magnitude and timing of the responses of the ocean and terrestrial components remain poorly constrained (33). Here, the word terrestrial includes both changes in biospheric productivity (respiration and photosynthesis) as well as biomass burning (fires). Following previous strong El Niño events (for example, the 1982-1983 and 1997-1998 El Niño events), methods for measuring the atmospheric CO<sub>2</sub> response to ENSO were based on *in situ* atmospheric CO<sub>2</sub> observations at a handful of surface stations that transect the tropical Pacific, including Mauna Loa, Christmas Island and American Samoa (8, 34) as well as shipboard transect measurements (12, 35-36). The annual growth rate of atmospheric CO<sub>2</sub> measured at these remote stations and other sites around the globe show remarkable correlation with ENSO indices, with a rapid increase in atmospheric CO<sub>2</sub> associated with the late stage of an El Niño event (19, 37). The ocean response to El Niño events is based on studies looking at *in situ* observations, for example, surface ocean *p*CO<sub>2</sub> observations from ships of opportunity (12), moorings (38-39), or targeted field campaigns during El Niño events (9-10, 40-41), and a variety of mechanistic ocean models (24, 52, 54, 61, 65, 67).

The overall increase in the release of CO<sub>2</sub> to the atmosphere during strong El Niño events has been attributed to a decrease in biospheric uptake of CO<sub>2</sub> (e.g., due to drying of tropical land regions and an increase in plant and soil respiration) combined with enhanced fire emissions. In recent years, this has led to a growing body of literature (42-49) concluding that ENSO-mediated variability in tropical net land primary productivity is what primarily influences the atmospheric CO<sub>2</sub> growth rate. A handful of studies (25, 50-51) have disputed any consistent or coherent response from the land component during El Niño events, thus highlighting the high level of uncertainty and disagreement within the carbon cycle community.



1       The El Niño-CO<sub>2</sub> signature should have a significant tropical Pacific Ocean component  
2 as well, with opposite sign to the terrestrial response (10, 13, 33). During strong El Niño events,  
3 there is a large-scale weakening of the easterly trade winds and suppression of eastern equatorial  
4 Pacific upwelling (indicated by a deeper thermocline) that reduces the supply of cold, carbon-  
5 rich waters to the surface (Fig. 1). This reduces the usual strong outgassing of CO<sub>2</sub> from this  
6 region (52-67), typically on the order of ~0.4–0.6 PgC yr<sup>-1</sup> to the atmosphere, by ~40-60%  
7 during an El Niño event (9-12, 33, 36, 60, 73). If net fluxes were to remain constant elsewhere,  
8 these substantial net air-sea CO<sub>2</sub> anomalies should lead to a reduction in the growth rate of  
9 atmospheric CO<sub>2</sub>, at least during the early stages of El Niño.

10       Understanding these variations in atmospheric CO<sub>2</sub>, the timing of these variations and the  
11 underlying processes that cause them have been of great interest within the carbon cycle  
12 community (1, 10-13, 15, 20, 33, 50). Integrating information from ocean- and atmosphere-based  
13 estimates, and modeling studies, we now know that it is the combined and opposite effect of  
14 ocean and terrestrial responses, which contribute to El Niño-related variations in atmospheric  
15 CO<sub>2</sub> (33). What remain controversial though are the timing of the ocean response and a precise  
16 quantification of its role. This is of crucial importance because typically the interannual  
17 variability (IAV) in the growth rate of atmospheric CO<sub>2</sub> is used to constrain the climate  
18 sensitivity of land carbon fluxes ( $\gamma_{LT}$ ) (20-21); however, if a component of the IAV is being  
19 modified by ocean fluxes, then these inferences of  $\gamma_{LT}$  need to be reconsidered.

20       Because of the few surface CO<sub>2</sub> monitoring stations over the center of action (i.e.,  
21 tropical Pacific Ocean), it has been challenging to directly observe the timing and changes in flux  
22 of CO<sub>2</sub> from the ocean to the atmosphere that affect the atmospheric CO<sub>2</sub> growth rate during an  
23 El Niño event. Efforts to analyze the data from distant measurement locations tend to identify the

enhanced CO<sub>2</sub> fluxes from the terrestrial carbon cycle, which dominate during the later stages of El Niño. The high-density, broad-scale observations of CO<sub>2</sub> from OCO-2 provide a valuable tool to partition the ocean and terrestrial carbon cycle responses to El Niño.

#### ***Time series of X<sub>CO2</sub> anomalies during the 2015-2016 El Niño***

OCO-2 observations describe the column-averaged CO<sub>2</sub> dry air mole fraction (X<sub>CO2</sub>). More details regarding the OCO-2 mission, data features, X<sub>CO2</sub> retrievals, etc. are provided in the Supplementary Materials, and are available in (69) and (70) while validation of X<sub>CO2</sub> via comparisons to a ground-based network are provided in (71).

El Niño events are identified by warm sea surface temperature anomalies in precise regions of the tropical Pacific Ocean, with the most commonly used being the Niño 3.4 region (5°S-5°N, 170°W-120°W). Figs. 2A and 2B show the trend in X<sub>CO2</sub> anomaly (90) for the Niño 3.4 region and its temporal evolution relative to two ENSO indices (91), including the Oceanic Niño Index (ONI - derived from sea surface temperature anomalies in the Niño 3.4 region) and the Southern Oscillation Index (SOI - derived from observed sea level pressure differences between Tahiti and Darwin, Australia). The 2015-2016 El Niño began around March 2015 and reached its peak over the Central Pacific between November 2015 and January 2016 (30). The X<sub>CO2</sub> anomaly (Fig. 2B) shows two distinct periods over the entire El Niño event: (a) Development phase of El Niño (Spring-Summer 2015) – we argue that the negative X<sub>CO2</sub> anomaly is due to a reduction in local CO<sub>2</sub> outgassing from the tropical Pacific Ocean, and (b) Mature phase of El Niño (Fall 2015 onwards) – we argue that the positive trend in X<sub>CO2</sub> anomaly reflects an increase in atmospheric CO<sub>2</sub> concentrations due to terrestrial sources (i.e., combination of reduced vegetation uptake across pan-tropical regions and enhanced biomass burning emissions from SE Asia and Indonesia). The time series in Fig. 2B shows the space-

1 based CO<sub>2</sub> dataset documenting the response of the carbon cycle (both oceanic and terrestrial)  
2 during an entire El Niño event, capturing both the development and the mature phase and the  
3 transition between those two. The timing of the OCO-2 launch was extremely fortuitous in this  
4 regard.

5 Deriving the X<sub>CO2</sub> anomalies require observations taken by both NASA's OCO-2 and the  
6 Japan Aerospace Exploration Agency's (JAXA) Greenhouse Gases Observing Satellite  
7 (GOSAT) (68) mission. The short OCO-2 record makes it impossible to fit a long-time series and  
8 calculate anomalies, and hence data from the GOSAT mission (operating since January 2009)  
9 was utilized to generate the X<sub>CO2</sub> climatology. The OCO-2 team retrieved X<sub>CO2</sub> from the first 7  
10 years of the GOSAT observations using the same retrieval algorithm that generated the OCO-2  
11 data product (90). Continuous global coverage from these two missions allows us to stitch  
12 together a long-time series of X<sub>CO2</sub> over remote regions, such as the tropical Pacific Ocean (Figs.  
13 S1-S2). However, utilizing two data sources, i.e., GOSAT and OCO-2, can incur errors in the  
14 analyses due to changes in the two instruments, their observing strategies and sampling density.  
15 Fig. 2B also illustrates the corresponding uncertainty in our analyses. The uncertainty is  
16 calculated using an ensemble technique (Section C in Supplementary Materials) and further  
17 brings out the two phases in the time series of the Niño 3.4 X<sub>CO2</sub> anomaly –  $\pm 0.3$  ppm  
18 uncertainties during the El Niño development phase with both the upper and lower bounds below  
19 the zero line, and larger uncertainties of  $\pm 0.5$  ppm during the mature phase of the El Niño event.  
20 These larger uncertainties during the latter stages of the El Niño illustrate the challenge in  
21 attributing the changes in X<sub>CO2</sub> anomalies to the competing, and often opposing, signals from the  
22 ocean and the terrestrial components of the carbon cycle.

1 *Attributing the two observed phases of  $X_{CO_2}$  anomalies to the ocean and the terrestrial*  
2 *response*

3 Our argument for the two observed phases in the  $X_{CO_2}$  anomaly time series is supported  
4 by complementary data sources. The ocean response is corroborated by sea surface  $pCO_2$   
5 observations from an *in situ* network of autonomous  $CO_2$  systems on the TAO moored buoy  
6 array (9, 38, 72). Data are not directly comparable to atmospheric  $X_{CO_2}$  as they describe  $CO_2$   
7 variations at the ocean surface. The trend of the difference between the sea surface and  
8 atmospheric  $CO_2$  ( $\Delta pCO_2$ ), however, does capture typical El Niño signatures. For example, Fig.  
9 2C illustrates data from one of the moored buoys in the Niño 3.4 region ( $0^\circ$ ,  $170^\circ W$ ), which  
10 shows decreasing  $\Delta pCO_2$  over the spring and near-zero  $\Delta pCO_2$  by December 2015. A  
11 suppression in the upwelling of  $CO_2$ -rich waters caused by weakening of the easterly trade winds  
12 leads to a reduction in the surface ocean carbon content, which in turn leads to a decline in the  
13 magnitude of sea-to-air  $CO_2$  fluxes. The flux estimates at this buoy location are  $1.35 \pm 0.21$  ( $1\sigma$ )  
14  $gC\ m^{-2}\ month^{-1}$  during the November 2014 to February 2015 period (i.e., non El Niño  
15 conditions) that gradually decrease to  $0.087 \pm 0.083$  ( $1\sigma$ )  $gC\ m^{-2}\ month^{-1}$  between November  
16 2015 and February 2016 (i.e., El Niño conditions). This indicates a near-total shutdown of sea-  
17 to-air flux during Boreal Winter 2015-2016 relative to the neutral 2014-2015 Boreal Winter.  
18 Previous studies focusing on the tropical Pacific Ocean have reported flux reductions of ~40-  
19 60% over the entire basin (9-12, 33, 36, 60, 73). Atmospheric transport model calculations with a  
20 prescribed set of flux patterns and comparing to the observed  $X_{CO_2}$  anomalies (Section A in  
21 Supplementary Materials) suggest a flux reduction of ~26-54%.

22 While these numbers are roughly similar, we do recognize the limitation in comparing  
23 flux estimates from one point (namely the TAO location at  $0^\circ$ ,  $170^\circ W$ ) to flux estimates for the

entire Niño 3.4 region and/or the tropical Pacific Ocean from previous studies. Large-scale changes in the physical and biogeochemical dynamics during El Niño events result in significant spatial and temporal variability in the surface  $p\text{CO}_2$  distributions (12, 62, 65). Additionally, these spatial variations and their seasonal progression are uniquely tied to each El Niño event; thus, different flavors of El Niño events and/or shifts in the El Niño phenomena (86-88) will influence the evolution of the seasonal cycle of  $p\text{CO}_2$  and air-sea  $\text{CO}_2$  fluxes over the region. For the 2015-2016 El Niño event, the TAO buoy at  $0^\circ$ ,  $170^\circ\text{W}$  lay closest to the edge of the warm pool and registered the first response to the onset of El Niño conditions. As observations from other TAO locations (92) are becoming available, it is evident that in the eastern part of the basin there was an overall suppression of the outgassing  $\text{CO}_2$  source but with large variability in  $p\text{CO}_2$ . Data synthesis and modeling work with these and other *in situ* observations are ongoing to quantify the exact magnitude of ocean  $\text{CO}_2$  fluxes over different tropical Pacific regions during the 2015-2016 El Niño.

The second phase in the  $X_{\text{CO}_2}$  anomaly time series is driven by the terrestrial component of the carbon cycle, and the transport of this signal to the remote Niño 3.4 region. The anomalous increase in  $\text{CO}_2$  can be attributed to a combination of terrestrial sources, including a reduction in the global biospheric uptake, increases in soil and plant respiration and enhanced fire emissions. In fact, the impact of enhanced fire emissions and their regional progression was a well-studied feature following the strong 1997-1998 El Niño (26, 43, 74-76). For the 2015-2016 El Niño event, strong correspondences between  $X_{\text{CO}_2}$  from OCO-2 and the carbon monoxide (CO) total column anomalies from the Measurements of Pollution in the Troposphere (MOPITT) instrument on the NASA Terra platform, are evident over the tropical Pacific Ocean, especially during Fall 2015 (Fig. 2D). We conjecture that these CO total column anomalies are

1 representative of the emissions from the 2015–2016 Indonesian peat fires (77-80), which were  
2 advected into the tropical Pacific region. El Niño-related changes in the Walker circulation (i.e.,  
3 westerly winds) and the slightly more southern than normal positioning of the Inter Tropical  
4 Convergence Zone (ITCZ) (81) may allow emissions from the Indonesian peat fires to carry over  
5 into this region (Fig. S4). It is interesting to note from Figs. 2B and 2D that the positive increase  
6 in  $X_{CO_2}$  anomaly actually leads the fire signals by 1-2 months. This indicates that the release of  
7 carbon flux resulting in an increase in  $CO_2$  concentrations is only partially pyrogenic; reduced  
8 vegetation uptake due to droughts is a significant contributor, and quite possibly the initial cause  
9 of the increase in  $X_{CO_2}$  anomaly.

#### 10 ***Isolating the observed negative $X_{CO_2}$ anomaly to an ocean signal***

11 The time dependence of the  $X_{CO_2}$  anomalies during the 2015-2016 El Niño indicate that  
12 the initial decrease in atmospheric  $CO_2$  is due to suppression of upwelling in the tropical Pacific.  
13 This early negative response is subsequently offset by a large positive anomaly due to the  
14 terrestrial component. Assuming no significant interannual changes elsewhere in the global  
15 ocean, we can further confirm our argument by a comparison of the  $X_{CO_2}$  anomaly in the Niño  
16 3.4 region with the global  $X_{CO_2}$  anomaly (Fig. 4A). By differencing the far-field effect from the  
17 local signal, the influence of the reduction in  $CO_2$  outgassing from the tropical Pacific Ocean is  
18 clearly visible during the onset phase of El Niño. The peak reduction registered over the Niño 3.4  
19 region relative to the global  $X_{CO_2}$  anomalies is 0.35 ppm in June 2015, which occurs a couple of  
20 months after the initiation of the El Niño event. Lag correlation of the Niño 3.4  $X_{CO_2}$  anomalies  
21 against the ONI index indicate that the highest positive correlation occurs when the  
22 concentration-related anomalies lag the SST-related anomalies by 1-2 months (93) (Fig. S8). The  
23 time lag relationship can be precisely quantified during the onset phase of El Niño, but it is much

1 more difficult to interpret during the succeeding El Niño stages when any reduction in CO<sub>2</sub> from  
2 decreased equatorial upwelling is masked by the signal from terrestrial processes. Thus, if it were  
3 not for the reduction in outgassing from the ocean, the impact from the terrestrial sources would  
4 likely be larger. Our analysis confirms the findings from (13) that the slowdown of atmospheric  
5 CO<sub>2</sub> increase during the early stages of an El Niño is indeed related to the decreased sea-to-air  
6 flux of CO<sub>2</sub> in the tropical Pacific Ocean. The coverage from the OCO-2 mission has enabled us  
7 to verify this hypothesis and monitor its temporal evolution using real atmospheric CO<sub>2</sub>  
8 observations.

9         The early stage negative X<sub>CO2</sub> anomaly is unique to the tropical Pacific Ocean and is not  
10 influenced by global, terrestrial or large-spatial scale fluxes. Due to the large interhemispheric  
11 gradients in CO<sub>2</sub>, typical variability in tropical CO<sub>2</sub> concentrations can be an aliasing of  
12 terrestrial processes occurring at higher latitudes. In order to confirm that the recovered ocean  
13 signal in the X<sub>CO2</sub> anomaly is unique to the tropical Pacific Ocean, we examined three other  
14 ocean regions - the subtropical North Pacific (20°-30°N, 120°-170°W), the subtropical South  
15 Pacific (20°-30°S, 120°-170°W) and the tropical Atlantic Ocean (5°N -5°S, 5°-35°W). Fig. 3  
16 shows the specific regions (aside from Niño 3.4) that we have analyzed, and each of which assist  
17 us to reject alternative hypotheses. Non-zero differences in X<sub>CO2</sub> anomalies between these and  
18 the Niño 3.4 region (Fig. 4) indicate that the trend observed over the tropical Pacific Ocean is  
19 distinct from other ocean basins. This makes intuitive sense from our mechanistic understanding  
20 as well - while large impacts of ENSO on the sea-to-air CO<sub>2</sub> flux in the tropical Pacific Ocean  
21 are expected, studies have shown minute and delayed influence of the ENSO modes on the  
22 variability of carbon fields in the tropical Atlantic Ocean (66, 82-83).

### 23 *Perspective*

1           The strong El Niño in 2015-2016 caused a reduction in the magnitude of CO<sub>2</sub> outgassing  
2 from the tropical Pacific Ocean. These changes, albeit of varying magnitude, extended over a  
3 large portion of the tropical Pacific, and impacted the large-scale modulation of the physical  
4 processes responsible for the CO<sub>2</sub> efflux from this region. Almost all observing networks (i.e.,  
5 OCO-2, TAO, etc.) were aided by the strength of this signal. However, OCO-2 provided a more  
6 comprehensive view of the tropical Pacific Ocean signal than previous observing networks given  
7 its: (a) greater coverage and more frequent sampling than *in situ* networks, and (b) improved  
8 resolution and precision than earlier space-based instruments. For example, GOSAT, like OCO-2  
9 is sensitive to the total CO<sub>2</sub> column, but has lower precision (2 ppm single sounding random  
10 error for GOSAT vs. 0.5 ppm for OCO-2) and lower sampling density (100x less soundings).  
11 The immediate next step will be to fold in these observations into an inverse modeling  
12 framework (13, 15, 50, 56) to infer the underlying net fluxes between the ocean and atmosphere  
13 and the terrestrial biosphere and the atmosphere. This would help establish the real benefit of  
14 OCO-2, especially against the backdrop of previous studies that had to rely on sparse  
15 atmospheric constraint to infer changes in CO<sub>2</sub> surface fluxes during El Niño events.

16           Based on OCO-2 data alone, however, we cannot quantitatively discriminate the relative  
17 roles of reduction in biospheric activity uptake due to a warmer and drier climate in 2015 versus  
18 enhanced fire emissions. While we can quantify the temporal response of the ocean versus the  
19 terrestrial component and qualitatively observe the gradients in the response of different tropical  
20 Pacific Ocean regions (Fig. 5), it is much more challenging to discriminate the contribution of  
21 fire emissions and the delayed response of the terrestrial biosphere to El Niño-induced changes  
22 in weather patterns. The impact of ENSO is typically felt by the terrestrial biosphere over several  
23 months to a year after the actual event. Studies on both progressions of droughts (84) and fires



(26) during an El Niño cycle have shown a hysteresis in the Earth system's response to changes in temperature and precipitation patterns. Analyses using ancillary data sources such as solar-induced fluorescence (SIF), bottom-up model simulations and inverse modeling calculations are typically necessary to quantify the partitioning of the terrestrial carbon fluxes (reduction in biospheric uptake vs. increase in fire emissions) as has been pursued in a companion study (85).

Our study provides a short-term perspective on the potential of CO<sub>2</sub> observations from space for unraveling more complex relationships of carbon sources and sinks in the future. A longer time series of observations will enable testing more hypotheses such as the possibility of regionally dependent gradients in air-sea CO<sub>2</sub> fluxes in the tropical Pacific, or adding data to support biogeochemical theories at previously inaccessible scales. From a long-term perspective, such information will improve our process-based understanding, inform our current suite of mechanistic models, and ultimately, better constrain future carbon cycle projections.

### ***Concluding remarks***

The strong El Niño event of 2015-2016 provided us with an opportunity to study how the global carbon cycle responds to changes in the physical climate system. With the high-resolution (both spatial and temporal) observations available from OCO-2, we are able to directly: (a) observe the strong correlations that exist between atmospheric CO<sub>2</sub> concentrations and the El Niño signal, and (b) track the development of the atmospheric CO<sub>2</sub> anomaly as it switches from a negative phase (i.e., due to a reduction in CO<sub>2</sub> outgassing from the tropical Pacific Ocean) to a strong positive phase (i.e., due to a reduction in biospheric uptake and increased fire emissions). The most important contribution of the space-based OCO-2 mission is the ability to observe and monitor carbon cycle phenomena at high-density over large spatial scales, which has not been possible from the existing *in situ* network.

1           The complexity of the El Niño – CO<sub>2</sub> signature illustrates that it is a multifaceted system  
2   with contributions from many regions and processes. Understanding and predicting its behavior  
3   requires separating out the many terrestrial and marine regions that contribute (1, 33) and  
4   identifying both the geophysical (3, 27, 30) and the biological (10, 59, 89) phenomena that  
5   respond in their own unique ways. However, the impact on the carbon cycle is unified through  
6   the global mixing of CO<sub>2</sub> in the atmosphere - OCO-2 makes a unique contribution by providing  
7   both the global coverage and fine surface spatial detail; alongside the *in situ* CO<sub>2</sub> network of  
8   moorings and shipboard measurements provide the long-term climate-quality record of  
9   atmospheric and ocean CO<sub>2</sub> observations and serves to validate the OCO-2 observations and  
10   model products. We emphasize that this diverse observing portfolio is necessary, and the  
11   complementary information provided by these observing systems will likely prove critical in  
12   understanding the partitioning of carbon fluxes during the 2015-2016 El Niño, the relative  
13   contribution of ocean vs. land to the global atmospheric CO<sub>2</sub> growth rate, and the sensitivity of  
14   the carbon cycle to climate forcing on interannual to decadal timescales.

## References and Notes:

1. M. J. McPhaden, S. E. Zebiak, M. H. Glantz, ENSO as an integrating concept in Earth science. *Science* **314**, 1740-1745 (2006).
2. S. G. Philander, *El Niño, La Niña, and the Southern Oscillation* (Academic Press, San Diego, CA, 1990).
3. J. D. Neelin *et al.*, ENSO theory. *Journal of Geophysical Research-Oceans* **103**, 14261-14290 (1998).
4. K. E. Trenberth, The definition of El Niño. *Bulletin of the American Meteorological Society* **78**, 2771-2777 (1997).
5. M. A. Cane, The evolution of El Niño, past and future. *Earth and Planetary Science Letters* **230**, 227-240 (2005).
6. R. B. Bacastow *et al.*, Atmospheric carbon-dioxide, the southern oscillation, and the weak 1975 El-Niño. *Science* **210**, 66-68 (1980).
7. C. D. Keeling, R. Revelle, Effects of El-Niño Southern Oscillation on the atmospheric content of carbon dioxide. *Meteoritics* **20**, 437-450 (1985).
8. C. D. Keeling *et al.*, Interannual extremes in the rate of rise of atmospheric carbon dioxide since 1980. *Nature* **375**, 666-670 (1995).
9. F. P. Chavez *et al.*, Biological and chemical response of the equatorial Pacific Ocean to the 1997-98 El Niño. *Science* **286**, 2126-2131 (1999).
10. R. A. Feely *et al.*, Influence of El Niño on the equatorial Pacific contribution to atmospheric CO<sub>2</sub> accumulation. *Nature* **398**, 597-601 (1999).

11. R. A. Feely *et al.*, Seasonal and interannual variability of CO<sub>2</sub> in the equatorial Pacific. *Deep-Sea Research Part II-Topical Studies in Oceanography* **49**, 2443-2469 (2002).
12. R. A. Feely *et al.*, Decadal variability of the air-sea CO<sub>2</sub> fluxes in the equatorial Pacific Ocean. *Journal of Geophysical Research-Oceans* **111**, 16 (2006).
13. P. J. Rayner, R. M. Law, R. Dargaville, The relationship between tropical CO<sub>2</sub> fluxes and the El Niño-Southern Oscillation. *Geophysical Research Letters* **26**, 493-496 (1999).
14. C. D. Jones *et al.*, The carbon cycle response to ENSO: A coupled climate-carbon cycle model study. *Journal of Climate* **14**, 4113-4129 (2001).
15. P. Peylin *et al.*, Multiple constraints on regional CO<sub>2</sub> flux variations over land and oceans. *Global Biogeochemical Cycles* **19**, 21 (2005).
16. K. R. Gurney *et al.*, Interannual variations in continental-scale net carbon exchange and sensitivity to observing networks estimated from atmospheric CO<sub>2</sub> inversions for the period 1980 to 2005. *Global Biogeochemical Cycles* **22**, 17 (2008).
17. C. D. Nevison *et al.*, Contribution of ocean, fossil fuel, land biosphere, and biomass burning carbon fluxes to seasonal and interannual variability in atmospheric CO<sub>2</sub>. *Journal of Geophysical Research-Biogeosciences* **113**, 21 (2008).
18. X. Jiang *et al.*, Interannual variability of mid-tropospheric CO<sub>2</sub> from Atmospheric Infrared Sounder. *Geophysical Research Letters* **37**, 5 (2010).
19. R. Betts *et al.*, El Niño and a record CO<sub>2</sub> rise. *Nature Climate Change* **6**, 806-810 (2016).
20. P. M. Cox *et al.*, Sensitivity of tropical carbon to climate change constrained by carbon dioxide variability. *Nature* **494**, 341-344 (2013).
21. S. Wenzel *et al.*, Emergent constraints on climate-carbon cycle feedbacks in the CMIP5

- 1 Earth system models. *Journal of Geophysical Research-Biogeosciences* **119**, 794–807  
2 (2014).
- 3 22. K. E. Trenberth *et al.*, Progress during TOGA in understanding and modeling global  
4 teleconnections associated with tropical sea surface temperatures. *Journal of Geophysical*  
5 *Research-Oceans* **103**, 14291–14324 (1998).
- 6 23. J. J. Tribbia, “The rudimentary theory of atmospheric teleconnections associated with  
7 ENSO” in *Teleconnections Linking Worldwide Climate Anomalies*, M. H. Glantz, R. W.  
8 Katz, and N. Nicholls, Eds. (Cambridge University Press, New York, 1991), pp 285–308.
- 9 24. L. Resplandy, R. Séférian, L. Bopp, Natural variability of CO<sub>2</sub> and O<sub>2</sub> fluxes: What can  
10 we learn from centuries-long climate models simulations? *Journal of Geophysical*  
11 *Research-Oceans* **120**, 384-404 (2015).
- 12 25. F. I. Woodward, M. R. Lomas, T. Quaife, Global responses of terrestrial productivity to  
13 contemporary climatic oscillations. *Philosophical Transactions of the Royal Society B-*  
14 *Biological Sciences* **363**, 2779-2785 (2008).
- 15 26. Y. Le Page *et al.*, Global fire activity patterns (1996-2006) and climatic influence: an  
16 analysis using the World Fire Atlas. *Atmospheric Chemistry and Physics* **8**, 1911-1924  
17 (2008).
- 18 27. M. J. McPhaden, COMMENTARY: Playing hide and seek with El Niño. *Nature Climate*  
19 *Change* **5**, 791–795 (2015).
- 20 28. A. F. Z. Levine, M. J. McPhaden, How the July 2014 easterly wind burst gave the 2015-  
21 2016 El Niño a head start. *Geophysical Research Letters* **43**, 6503 – 6510 (2016).
- 22 29. F. Gasparin, D. Roemmich, The strong freshwater anomaly during the onset of the  
23 2015/2016 El Niño. *Geophysical Research Letters* **43**, 6452 – 6460 (2016).

- 1 30. H. Paek, J. -Y. Yu, C. Qian, Why were the 2015/2016 and 1997/1998 extreme El Niños  
2 different? *Geophysical Research Letters* **44**, 1848-1856 (2017).
- 3 31. R. B. Bacastow, Modulation of atmospheric carbon dioxide by southern  
4 oscillation. *Nature* **261**, 116-118 (1976).
- 5 32. R. E. Newell, B. C. Weare, A relationship between atmospheric carbon dioxide and  
6 Pacific sea surface temperatures. *Geophysical Research Letters* **4**, 1–2 (1977).
- 7 33. J. L. Sarmiento, N. Gruber, “Carbon Cycle, CO<sub>2</sub> and Climate” in Ocean Biogeochemical  
8 Dynamics (Princeton University Press, Princeton, NJ, 2006) pp. 392-453.
- 9 34. A. C. Manning *et al.*, Interpreting the seasonal cycles of atmospheric oxygen and carbon  
10 dioxide concentrations at American Samoa Observatory. *Geophysical Research*  
11 *Letters* **30**, 4 (2003).
- 12 35. R. A. Feely *et al.*, Effects of wind speed and gas exchange parameterizations on the air-  
13 sea CO<sub>2</sub> fluxes in the equatorial Pacific Ocean. *Journal of Geophysical Research-*  
14 *Oceans* **109**, 10 (2004).
- 15 36. M. Ishii *et al.*, Air-sea CO<sub>2</sub> flux in the Pacific Ocean for the period 1990-  
16 2009. *Biogeosciences* **11**, 709-734 (2014).
- 17 37. C. D. Jones, P. M. Cox, On the significance of atmospheric CO<sub>2</sub> growth rate anomalies  
18 in 2002-2003. *Geophysical Research Letters* **32**, 4 (2005).
- 19 38. A. J. Sutton *et al.*, Natural variability and anthropogenic change in equatorial Pacific  
20 surface ocean pCO<sub>2</sub> and pH. *Global Biogeochemical Cycles* **28**, 131-145 (2014).
- 21 39. A. J. Sutton *et al.*, A high-frequency atmospheric and seawater pCO<sub>2</sub> data set from 14  
22 open-ocean sites using a moored autonomous system. *Earth System Science Data* **6**, 353-  
23 366 (2014).

- 1 40. R. A. Feely *et al.*, Distribution of chemical tracers in the eastern equatorial pacific  
2 during and after the 1982-1983 El Niño southern oscillation event. *Journal of*  
3 *Geophysical Research-Oceans* **92**, 6545-6558 (1987).
- 4 41. R. A. Feely *et al.*, Variability of CO<sub>2</sub> distributions and sea-air fluxes in the central and  
5 eastern equatorial Pacific during the 1991-1994 El Niño. *Deep-Sea Research Part II-*  
6 *Topical Studies in Oceanography* **44**, 1851-1867 (1997).
- 7 42. H. Hashimoto *et al.*, El Niño-Southern Oscillation-induced variability in terrestrial  
8 carbon cycling. *Journal of Geophysical Research-Atmospheres* **109**, 8 (2004).
- 9 43. P. K. Patra *et al.*, Role of biomass burning and climate anomalies for land-atmosphere  
10 carbon fluxes based on inverse modeling of atmospheric CO<sub>2</sub>. *Global Biogeochemical*  
11 *Cycles* **19**, 10 (2005).
- 12 44. G. R. van der Werf *et al.*, Interannual variability in global biomass burning emissions  
13 from 1997 to 2004. *Atmospheric Chemistry and Physics* **6**, 3423-3441 (2006).
- 14 45. H. Qian, R. Joseph, N. Zeng, Response of the terrestrial carbon cycle to the El Niño-  
15 Southern Oscillation. *Tellus Series B-Chemical and Physical Meteorology* **60**, 537-550  
16 (2008).
- 17 46. W. H. Li *et al.*, Impact of two different types of El Niño events on the Amazon climate  
18 and ecosystem productivity. *Journal of Plant Ecology* **4**, 91-99 (2011).
- 19 47. T. Iguchi, Correlations between interannual variations of simulated global and regional  
20 CO<sub>2</sub> fluxes from terrestrial ecosystems and El Niño Southern Oscillation. *Tellus Series*  
21 *B-Chemical and Physical Meteorology* **63**, 196-204 (2011).

- 1 48. W. L. Wang *et al.*, Variations in atmospheric CO<sub>2</sub> growth rates coupled with tropical  
2 temperature. *Proceedings of the National Academy of Sciences of the United States of*  
3 *America* **110**, 13061-13066 (2013).
- 4 49. W. R. L. Anderegg *et al.*, Tropical nighttime warming as a dominant driver of variability  
5 in the terrestrial carbon sink. *Proceedings of the National Academy of Sciences of the*  
6 *United States of America* **112**, 15591-15596 (2015).
- 7 50. P. Bousquet *et al.*, Regional changes in carbon dioxide fluxes of land and oceans since  
8 1980. *Science* **290**, 1342-1346 (2000).
- 9 51. C. R. Schwalm *et al.*, Does terrestrial drought explain global CO<sub>2</sub> flux anomalies  
10 induced by El Niño? *Biogeosciences* **8**, 2493-2506 (2011).
- 11 52. A. M. E. Winguth *et al.*, El Niño Southern Oscillation related fluctuations of the marine  
12 carbon cycle. *Global Biogeochemical Cycles* **8**, 39-63 (1994).
- 13 53. R. A. Feely *et al.*, CO<sub>2</sub> distributions in the equatorial Pacific during the 1991–1992  
14 ENSO event. *Deep-Sea Research Part II-Topical Studies in Oceanography* **42**, 365–386  
15 (1995).
- 16 54. C. Le Quere *et al.*, Interannual variability of the oceanic sink of CO<sub>2</sub> from 1979 through  
17 1997. *Global Biogeochemical Cycles* **14**, 1247-1265 (2000).
- 18 55. M. J. Behrenfeld *et al.*, Biospheric primary production during an ENSO  
19 transition. *Science* **291**, 2594-2597 (2001).
- 20 56. G. A. McKinley *et al.*, Pacific dominance to global air-sea CO<sub>2</sub> flux variability: A novel  
21 atmospheric inversion agrees with ocean models. *Geophysical Research Letters* **31**, 4  
22 (2004).



- 1 57. T. Takahashi *et al.*, Climatological mean and decadal change in surface ocean  $p\text{CO}_2$ , and  
2 net sea-air  $\text{CO}_2$  flux over the global oceans. *Deep-Sea Research Part II-Topical Studies*  
3 *in Oceanography* **56**, 554-577 (2009).
- 4 58. G. H. Park *et al.*, Variability of global net sea-air  $\text{CO}_2$  fluxes over the last three decades  
5 using empirical relationships. *Tellus Series B-Chemical and Physical Meteorology* **62**,  
6 352-368 (2010).
- 7 59. M. M. Gierach *et al.*, Biological response to the 1997-98 and 2009-10 El Niño events in  
8 the equatorial Pacific Ocean. *Geophysical Research Letters* **39**, 6 (2012).
- 9 60. R. Wanninkhof *et al.*, Global ocean carbon uptake: magnitude, variability and  
10 trends. *Biogeosciences* **10**, 1983-2000 (2013).
- 11 61. M. C. Long *et al.*, Twentieth-Century Oceanic Carbon Uptake and Storage in  
12 CESM1(BGC). *Journal of Climate* **26**, 6775-6800 (2013).
- 13 62. P. Landschützer *et al.*, Recent variability of the global ocean carbon sink. *Global*  
14 *Biogeochemical Cycles* **28**, 927–949 (2014).
- 15 63. P. Landschützer, N. Gruber, D. C. E. Bakker, Decadal variations and trends of the global  
16 ocean carbon sink. *Global Biogeochemical Cycles* **30**, 1-22 (2016).
- 17 64. C. Rödenbeck *et al.*, Interannual sea-air  $\text{CO}_2$  flux variability from an observation-driven  
18 ocean mixed-layer scheme. *Biogeosciences* **11**, 4599–4613 (2014).
- 19 65. V. K. Valsala *et al.*, Spatiotemporal characteristics of seasonal to multidecadal  
20 variability of  $p\text{CO}_2$  and air-sea  $\text{CO}_2$  fluxes in the equatorial Pacific Ocean. *Journal of*  
21 *Geophysical Research-Oceans* **119**, 8987-9012 (2014).

66. X. J. Wang *et al.*, Seasonal to decadal variations of sea surface  $p\text{CO}_2$  and sea-air  $\text{CO}_2$  flux in the equatorial oceans over 1984-2013: A basin-scale comparison of the Pacific and Atlantic Oceans. *Global Biogeochemical Cycles* **29**, 597-609 (2015).
67. A. Obata, Y. Kitamura, Interannual variability of the sea-air exchange of  $\text{CO}_2$  from 1961 to 1998 simulated with a global ocean circulation-biogeochemistry model. *Journal of Geophysical Research* **108**, 3337 (2003).
68. A. Kuze *et al.*, Thermal and near infrared sensor for carbon observation Fourier-transform spectrometer on the Greenhouse Gases Observing Satellite for greenhouse gases monitoring. *Applied Optics* **48**, 6716-6733 (2009).
69. D. Crisp *et al.*, The on-orbit performance of the Orbiting Carbon Observatory-2 (OCO-2) instrument and its radiometrically calibrated products. *Atmospheric Measurement Techniques* **10**, 59-81 (2017).
70. A. E. Eldering *et al.*, The Orbiting Carbon Observatory-2: first 18 months of science data products. *Atmospheric Measurement Techniques* **10**, 549-563, (2017).
71. D. Wunch *et al.*, Comparisons of the Orbiting Carbon Observatory-2 (OCO-2)  $\text{X}_{\text{CO}_2}$  measurements with TCCON. *Atmospheric Measurement Techniques* **10**, 2209-2238, (2017).
72. M. J. McPhaden *et al.*, The tropical ocean global atmosphere observing system: A decade of progress. *Journal of Geophysical Research-Oceans* **103**, 14169-14240 (1998).
73. T. Takahashi *et al.*, Decadal variation of the surface water  $p\text{CO}_2$  in the western and central equatorial Pacific. *Science* **302**, 852–856 (2003).
74. S. E. Page *et al.*, The amount of carbon released from peat and forest fires in Indonesia during 1997. *Nature* **420**, 61-65 (2002).

- 1 75. R. L. Langenfelds *et al.*, Interannual growth rate variations of atmospheric CO<sub>2</sub> and its  
2 delta C-13, H-2, CH<sub>4</sub>, and CO between 1992 and 1999 linked to biomass burning.  
3 *Global Biogeochemical Cycles* **16**, 1048-1069 (2002).
- 4 76. G. R. van der Werf *et al.*, Continental-scale partitioning of fire emissions during the  
5 1997 to 2001 El Niño/La Nina period. *Science* **303**, 73-76 (2004).
- 6 77. R. J. Parker *et al.*, Atmospheric CH<sub>4</sub> and CO<sub>2</sub> enhancements and biomass burning  
7 emission ratios derived from satellite observations of the 2015 Indonesian fire plumes.  
8 *Atmospheric Chemistry and Physics* **16**, 10111-10131 (2016).
- 9 78. V. Huijnen *et al.*, Fire carbon emissions over maritime southeast Asia in 2015 largest  
10 since 1997. *Scientific Reports* **6**, 8 (2016).
- 11 79. R. D. Field *et al.*, Indonesian fire activity and smoke pollution in 2015 show persistent  
12 nonlinear sensitivity to El Niño-induced drought. *Proceedings of the National Academy*  
13 *of Sciences of the United States of America* **113**, 9204-9209 (2016).
- 14 80. Y. Yin *et al.*, Variability of fire carbon emissions in equatorial Asia and its nonlinear  
15 sensitivity to El Niño. *Geophysical Research Letters* **43**, 10472–10479 (2016).
- 16 81. T. Schneider, T. Bischoff, G. H. Haug, Migrations and dynamics of the intertropical  
17 convergence zone. *Nature* **513**, 45-53 (2014).
- 18 82. G. A. McKinley *et al.*, Convergence of atmospheric and North Atlantic carbon dioxide  
19 trends on multidecadal timescales. *Nature Geoscience* **4**, 606-610 (2011).
- 20 83. N. Lefèvre, G. Caniaux, S. Janicot, A. K. Gueye, Increased CO<sub>2</sub> outgassing in February-  
21 May 2010 in the tropical Atlantic following the 2009 Pacific El Niño. *Journal of*  
22 *Geophysical Research-Oceans* **118**, 1645–1657 (2013).

84. S. M. Vicente-Serrano *et al.*, A multiscale global evaluation of the impact of ENSO on droughts. *Journal of Geophysical Research-Atmospheres* **116**, 23 (2011).
85. J. Liu *et al.*, Contrasting carbon cycle responses of the tropical continents to the 2015 El Niño. *Science* **THIS ISSUE**, xx (xxxx)
86. J. – S. Kug, F. F. Jin, S. An, Two types of El Niño events: cold tongue El Niño and warm pool El Niño. *Journal of Climate* **22**, 1499–1515 (2009).
87. K. Ashok, T. Yamagata, The El Niño with a difference. *Nature* **461**, 481-484 (2009).
88. M. J. McPhaden, T. Lee, D. McClurg, El Niño and its relationship to changing background conditions in the tropical Pacific Ocean. *Geophysical Research Letters* **38**, L15709 (2011).
89. C. Pala, CLIMATE Corals tie stronger El Niños to climate change. *Science* **354**, 1210 (2016).
90. Procedure for generating the X<sub>CO2</sub> climatology, calculating the anomaly, sensitivity tests to ascertain its robustness, and associated caveats are described in the Materials and Methods in the Supplementary Materials.
91. See the full list at - <http://www.esrl.noaa.gov/psd/data/climateindices/list/>
92. Data from other TAO locations (for example, at 0°, 110°W) demonstrate the heterogeneity in CO<sub>2</sub> concentrations as we move from west-to-east over the tropical Pacific Ocean. These data can be viewed at - <http://www.pmel.noaa.gov/co2/story/OpenOceanMoorings>
93. Bacastow (31) found the lag between one of the El Niño indices (SOI) and the CO<sub>2</sub> concentration changes to be 2.5 months at Mauna Loa and 6 months at South Pole. Rayner *et al.* (13) found in their study that CO<sub>2</sub> data anomalies lag the SOI by one month.

- 1 Later Jones *et al.* (14) claimed that Mauna Loa CO<sub>2</sub> lagged behind Niño 3 SST anomalies  
2 by 3 months. The handful of studies illustrate the range of ENSO indices and atmospheric  
3 CO<sub>2</sub> dataset that have been employed; however, all of these studies were impacted by a  
4 lack of broad-scale observations over the tropical Pacific during the different phases of an  
5 El Niño event. This study provides a refinement of these earlier estimates of the time lags  
6 using higher-density space-based observations.
- 7 94. D. Crisp *et al.*, The orbiting carbon observatory (OCO) mission. *Trace Constituents in*  
8 *the Troposphere and Lower Stratosphere* **34**, 700-709 (2004).
- 9 95. R. Pollock *et al.*, The Orbiting Carbon Observatory instrument: performance of the OCO  
10 instrument and plans for the OCO-2 instrument. *Proc. SPIE 7826, Sensors, Systems and*  
11 *Next Generation Satellites – XIV* **78260W** (2010).
- 12 96. T. E. Taylor *et al.*, Orbiting Carbon Observatory-2 (OCO-2) cloud screening algorithms:  
13 validation against collocated MODIS and CALIOP data. *Atmospheric Measurement*  
14 *Techniques* **9**, 973–989 (2016).
- 15 97. R. Nelson *et al.*, The potential of clear-sky carbon dioxide satellite retrievals.  
16 *Atmospheric Measurement Techniques* **9**, 1671–1684 (2016).
- 17 98. C. O'Dell *et al.*, The ACOS CO<sub>2</sub> retrieval algorithm – Part 1: Description and validation  
18 against synthetic observations. *Atmospheric Measurement Techniques* **5**, 99-121  
19 (2012).
- 20 99. D. Crisp *et al.*, The ACOS CO<sub>2</sub> retrieval algorithm--Part II: Global X<sub>CO2</sub> data  
21 characterization. *Atmospheric Measurement Techniques* **5**, 687–707 (2012).
- 22 100. J. Worden *et al.*, Evaluation, Validation, And Attribution Of OCO-2 X<sub>CO2</sub>  
23 Uncertainties. *Atmos. Meas. Tech. Disc.* Available at doi:10.5194/amt-2016-175, in

- review (2016).
101. H. Lindqvist *et al.*, Does GOSAT capture the true seasonal cycle of carbon dioxide? *Atmospheric Chemistry and Physics* **15**, 13023–13040 (2015).
102. O. Schneising *et al.*, Long-term analysis of carbon dioxide and methane column-averaged mole fractions retrieved from SCIAMACHY. *Atmospheric Chemistry and Physics* **11**, 2863–2880 (2011).
103. J. P. F. Fortuin, H. Kelder, An ozone climatology based on ozonesonde and satellite measurements. *Journal of Geophysical Research-Atmospheres* **103**, 31709 – 31734 (1998).
104. W. J. Randel, F. Wu, A stratospheric ozone profile data set for 1979–2005: Variability, trends, and comparisons with column ozone data. *Journal of Geophysical Research-Atmospheres* **112**, D06313 (2007).
105. R. D. McPeters, G. J. Labow, Climatology 2011: An MLS and sonde derived ozone climatology for satellite retrieval algorithms. *Journal of Geophysical Research-Atmospheres* **117**, D10303 (2012).
106. H. Nguyen, N. Cressie, A. Braverman, Multivariate Spatial Data Fusion for Very Large Remote Sensing Datasets. *Remote Sensing* **9**, 142 (2017).
107. R. F. Weiss, Carbon dioxide in water and seawater: the solubility of a non-ideal gas. *Marine Chemistry* **2**, 203–215 (1974).
108. M. N. Deeter *et al.*, Operational carbon monoxide retrieval algorithm and selected results for the MOPITT instrument. *Journal of Geophysical Research-Atmospheres* **108**, 4399 (2003).

- 1 109. L. Emmons *et al.*, Validation of Measurements of Pollution in the Troposphere  
2 (MOPITT) CO retrievals with aircraft in situ profiles. *Journal of Geophysical Research-*  
3 *Atmospheres* **109**, 13 (2004).
- 4 110. H. M. Worden *et al.*, Decadal record of satellite carbon monoxide  
5 observations. *Atmospheric Chemistry and Physics* **13**, 837-850 (2013).
- 6 111. Y. Yin *et al.*, Decadal trends in global CO emissions as seen by MOPITT.  
7 *Atmospheric Chemistry and Physics* **15**, 13433-13451 (2015).
- 8 112. M. N. Deeter *et al.*, The MOPITT Version 6 product: algorithm enhancements  
9 and validation. *Atmospheric Measurement Techniques* **7**, 3623-3632 (2014).
- 10 113. M. N. Deeter *et al.*, Validation and analysis of MOPITT CO observations of the  
11 Amazon Basin. *Atmospheric Measurement Techniques* **9**, 3999-4012 (2016).
- 12 114. J. F. Lamarque *et al.*, Identification of CO plumes from MOPITT data:  
13 Application to the August 2000 Idaho-Montana forest fires. *Geophysical Research*  
14 *Letters* **30**, 1688 (2003).
- 15 115. A. Arellano *et al.*, Time-dependent inversion estimates of global biomass-burning  
16 CO emissions using Measurement of Pollution in the Troposphere (MOPITT)  
17 measurements. *Journal of Geophysical Research-Atmospheres* **111**, D09303 (2006).
- 18 116. Z. Jiang *et al.*, Impact of model errors in convective transport on CO source  
19 estimates inferred from MOPITT CO retrievals. *Journal of Geophysical Research-*  
20 *Atmospheres* **118**, 2073–2083 (2013).
- 21 117. J. Worden *et al.*, El Niño, the 2006 Indonesian peat fires, and the distribution of  
22 atmospheric methane. *Geophysical Research Letters* **40**, 4938-4943 (2013).
- 23 118. R. Wanninkhof, Relationship between the wind speed and gas exchange over the

- ocean revisited. *Limnology and Oceanography - Methods* **12**, 351-362 (2014).
119. M. G. Bosilovich *et al.*, “MERRA-2: File Specification” (Tech. Rep. Global Modeling and Assimilation Office, Office Note No. 9, 2016).
120. K. R. Gurney *et al.*, TransCom 3 CO<sub>2</sub> inversion intercomparison: 1. Annual mean control results and sensitivity to transport and prior flux information. *Tellus Series B-Chemical and Physical Meteorology* **55**, 555-579 (2003).
121. K. R. Gurney *et al.*, Towards robust regional estimates of CO<sub>2</sub> sources and sinks using atmospheric transport models. *Nature* **415**, 626-630 (2002).
122. P. A. Pickers, A. C. Manning, Investigating bias in the application of curve fitting programs to atmospheric time series. *Atmospheric Measurement Techniques* **8**, 1469-1489 (2015).
123. K. W. Thoning, P. P. Tans, W. D. Komhyr, Atmospheric carbon dioxide at Mauna Loa Observatory, 2. Analysis of the NOAA/GMCC data, 1974-1985. *Journal of Geophysical Research-Atmospheres* **94**, 8549-8565 (1989).
124. W. Ebisuzaki, A Method to Estimate the Statistical Significance of a Correlation When the Data Are Serially Correlated. *Journal of Climate* **10**, 2147-2153 (1997).



## 1   **Acknowledgements:**

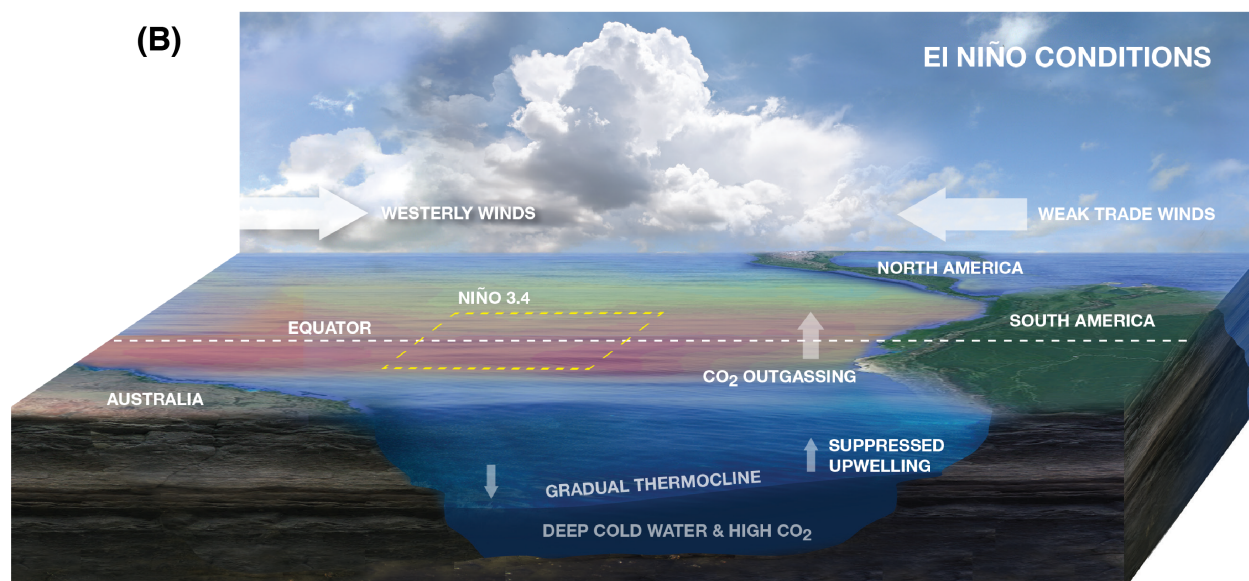
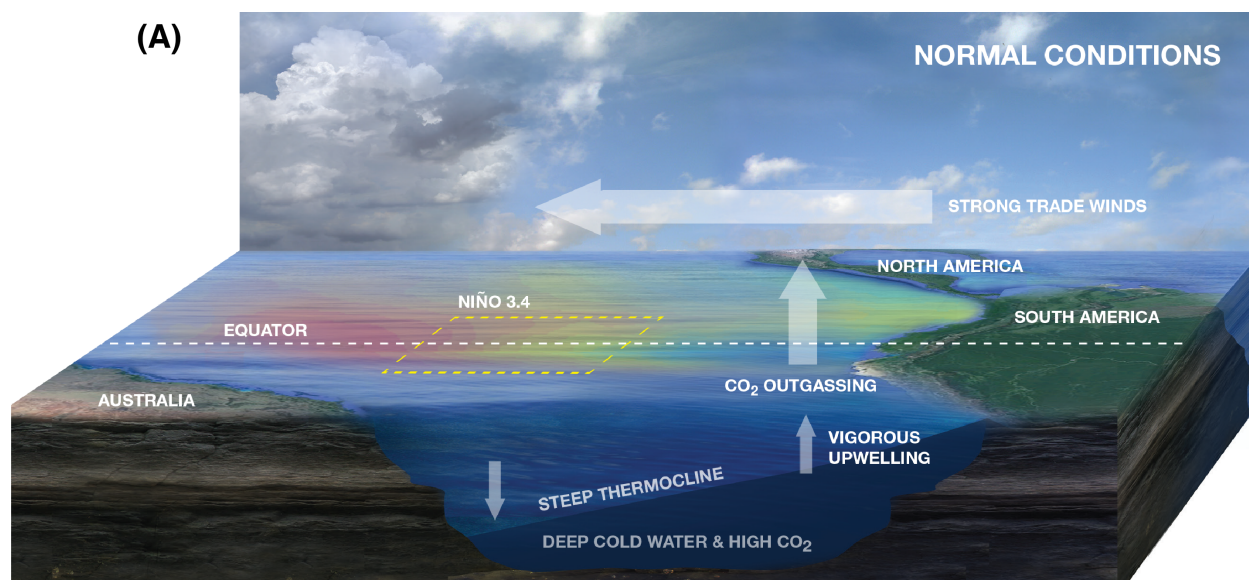
2           This work was supported by funding from the NASA ROSES-2014 Grant/Cooperative  
3   Agreement Number NNX15AG92G. A portion of this research was carried out at the Jet  
4   Propulsion Laboratory, California Institute of Technology, under a contract with the National  
5   Aeronautics and Space Administration. The work of B.B.S was supported by NCAR, which is  
6   sponsored by the National Science Foundation. The work of A.J.S. and R.A.F. was funded by the  
7   Office of Oceanic and Atmospheric Research (OAR) of the National Oceanic and Atmospheric  
8   Administration (NOAA), U.S. Department of Commerce, including resources from the Ocean  
9   Observation and Monitoring Division (OOMD) of the Climate Program Office (FundRef number  
10   100007298). This is Pacific Marine Environmental Laboratory Contribution No. 4607.

11           The OCO-2 and GOSAT-ACOS data were produced by the ACOS/OCO-2 project at the  
12   Jet Propulsion Laboratory, California Institute of Technology, and obtained from the free  
13   ACOS/OCO-2 data archive maintained at the NASA Goddard Earth Science Data and  
14   Information Services Center (<https://disc.gsfc.nasa.gov/OCO-2>). The MOPITT datasets were  
15   obtained from the NASA Langley Research Center Atmospheric Science Data Center  
16   ([https://eosweb.larc.nasa.gov/project/mopitt/mopitt\\_table](https://eosweb.larc.nasa.gov/project/mopitt/mopitt_table)). The authors gratefully acknowledge  
17   the National Data Buoy Center for supporting deployment and recovery of the moored  $p\text{CO}_2$   
18   systems and maintenance of the TAO buoys.

19           Finally, the authors would like to acknowledge the comments from the editor and three  
20   anonymous reviewers, discussions with Helen Worden (NCAR), John Worden (JPL), Paul  
21   Wennberg (Caltech), Steven Pawson (NASA), Stephen Cohn (NASA), Lesley Ott (NASA) and  
22   Brad Weir (USRA), and graphic design help from David Hinkle (JPL) and Sterling Spangler  
23   (SSAI).

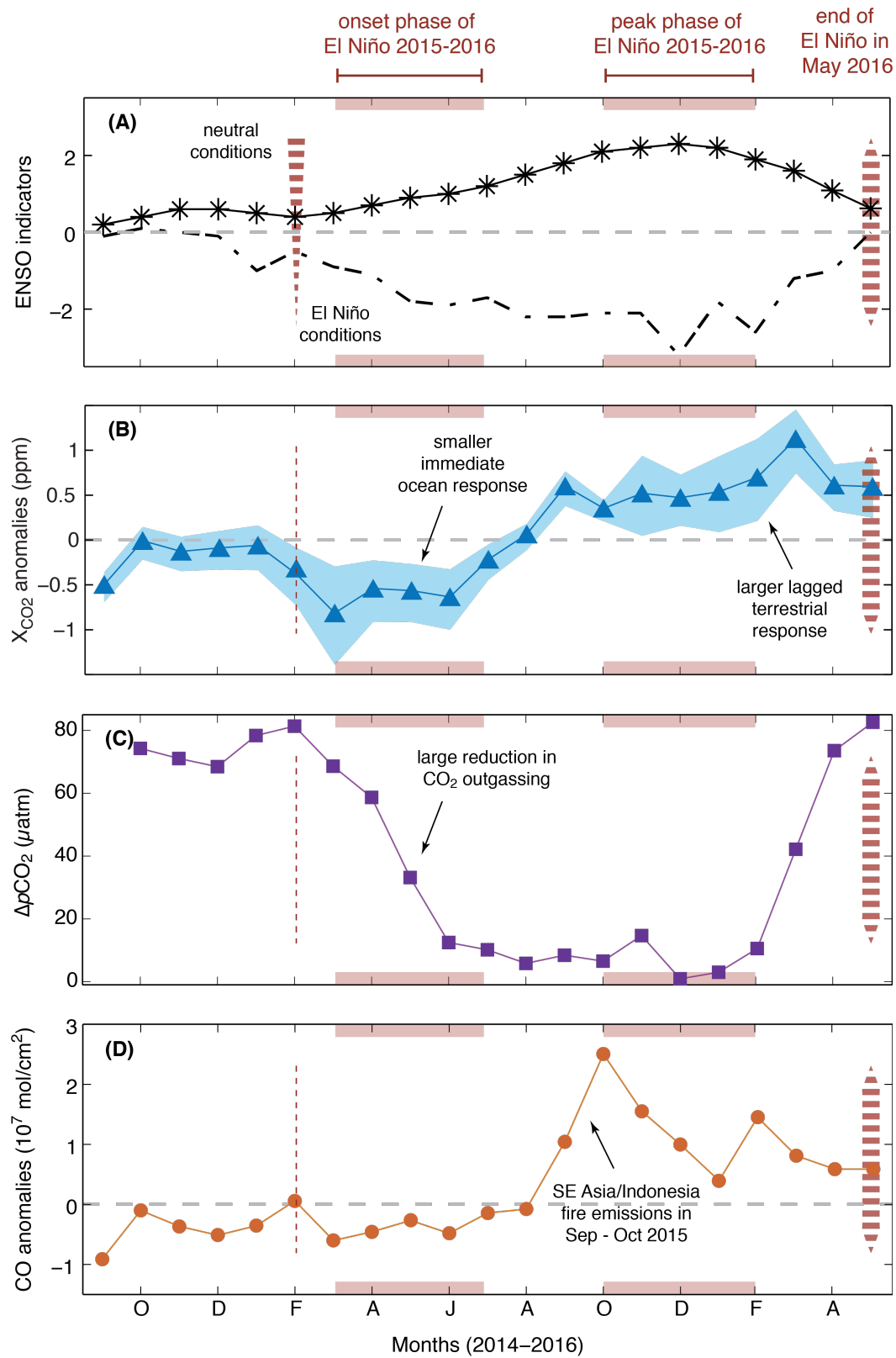
1 **Figures:**

2

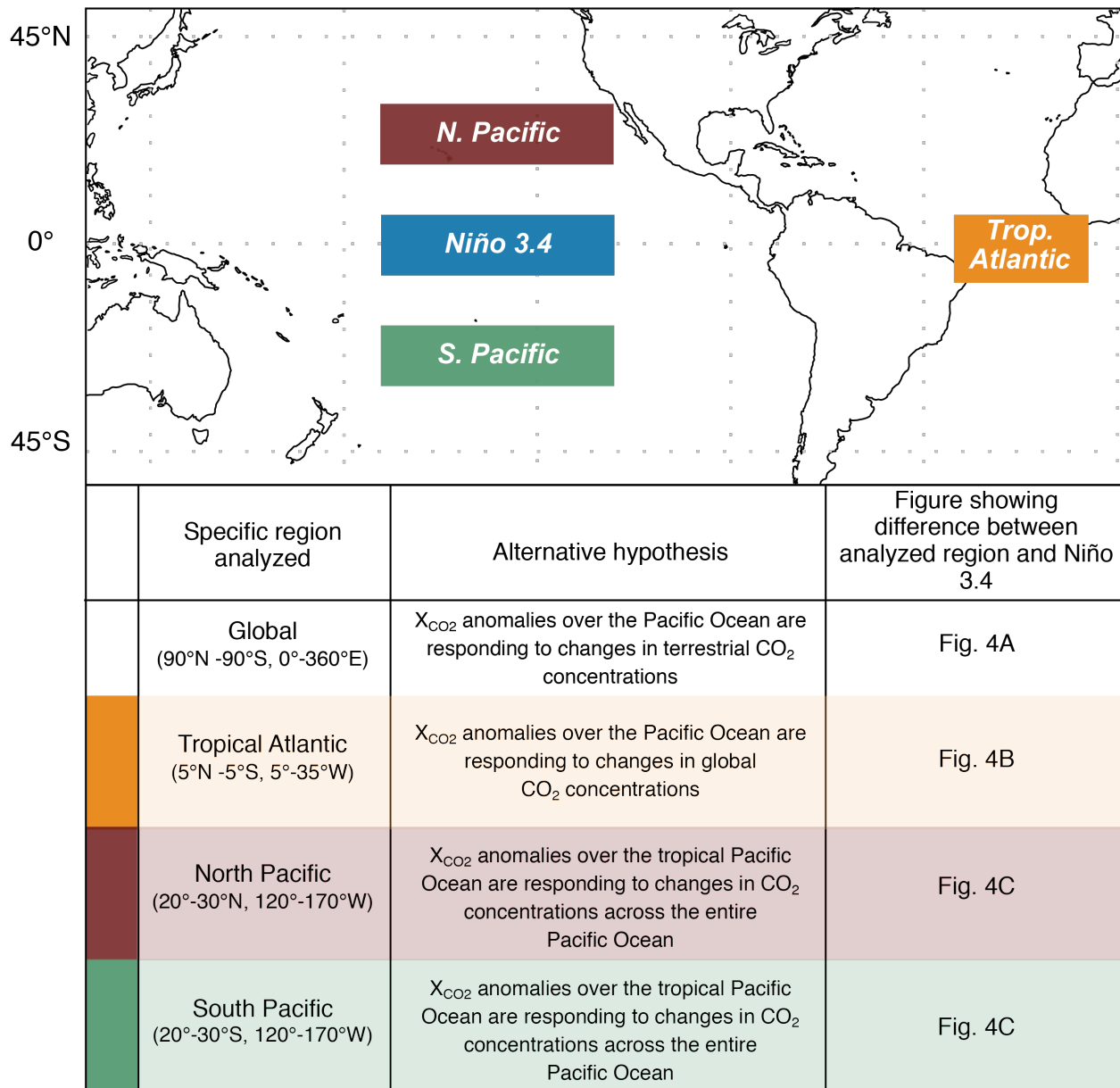


3

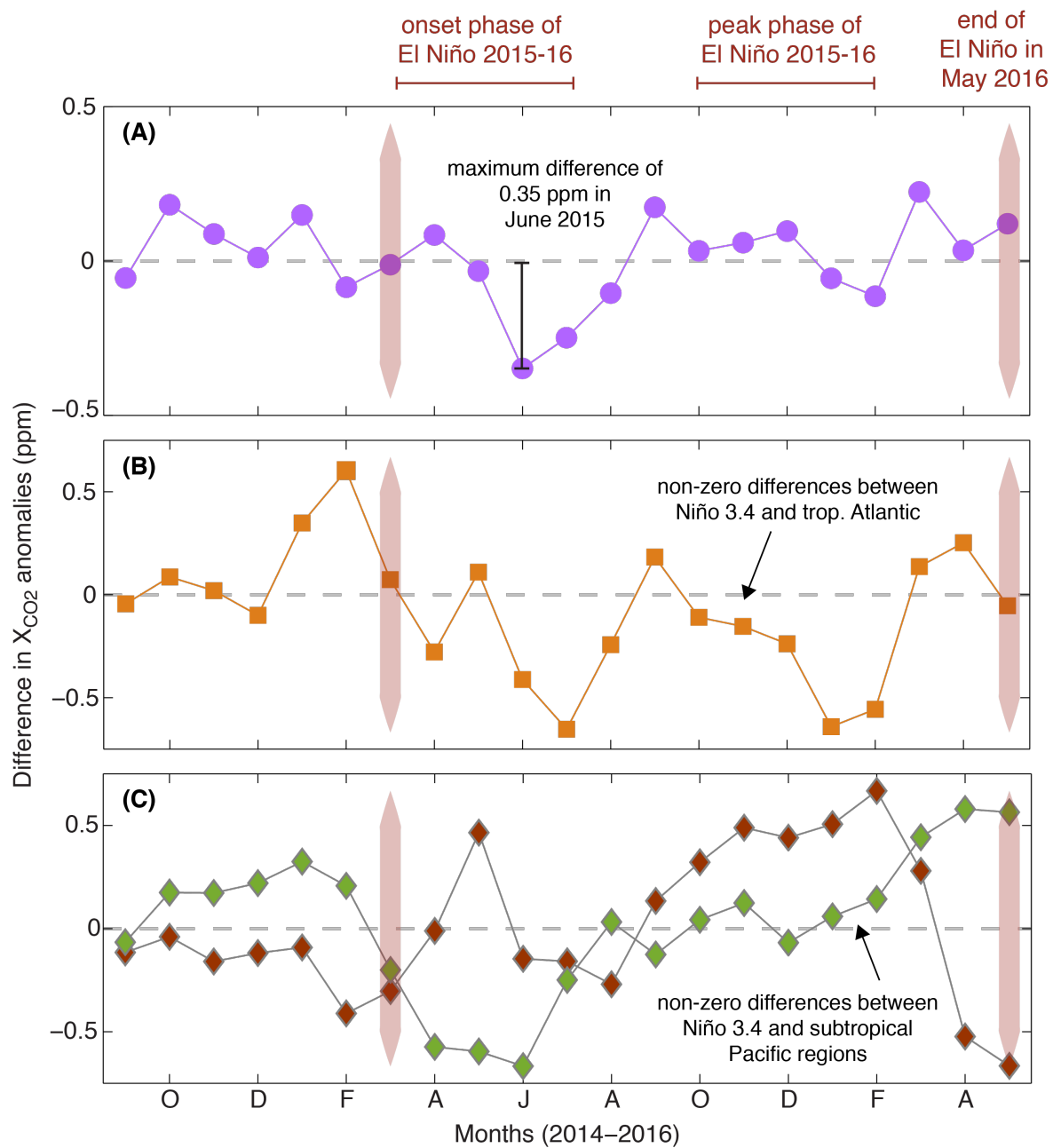
1 **Fig. 1.** Schematic of the mechanistic differences between normal (A) and El Niño (B) conditions  
2 and associated carbon response over the tropical Pacific Ocean. Warm ocean surface  
3 temperatures are denoted in red and cooler waters in blue. During El Niño conditions, easterly  
4 trade winds weaken and westerly wind bursts occur. In association with the shift in wind  
5 regimes, the western tropical Pacific warm pool moves eastward and the slope of the thermocline  
6 flattens in the central and eastern tropical Pacific. This suppresses upwelling of cold, carbon-rich  
7 waters in the central and eastern tropical Pacific, reducing the magnitude of CO<sub>2</sub> outgassing into  
8 the atmosphere. Also shown are changes in atmospheric convection, wherein convection shifts  
9 eastward in response to eastward displacement of western tropical Pacific warm pool waters.



1    **Fig. 2.** OCO-2 observes the response of the carbon cycle for an entire El Niño event. Temporal  
2    evolution of (A) the 2015-2016 El Niño as captured by the ONI and the SOI indices, (B)  $X_{\text{CO}_2}$   
3    anomalies and associated uncertainties in the Niño 3.4 region, (C)  $\Delta p\text{CO}_2$  from the TAO  $0^\circ$ ,  
4     $170^\circ\text{W}$  mooring, and (D) the CO total column anomalies in the Niño 3.4 region.



1 **Fig. 3.** Schematic showing the specific ocean basins (Niño 3.4, N. Pacific, S. Pacific and Trop.  
2 Atlantic) that were analyzed in this study.  $X_{CO_2}$  anomalies are calculated for these different ocean  
3 basins, and subsequently compared to the  $X_{CO_2}$  anomalies from the Niño 3.4 region. Each of  
4 these regions was considered to accept/reject a specific hypothesis that could potentially bias the  
5 observed trend in the Niño 3.4  $X_{CO_2}$  anomalies. After rejecting these hypotheses, we conclude  
6 that the negative  $X_{CO_2}$  anomaly observed over the Niño 3.4 during the onset phase of El Niño  
7 2015-2016 is unique and has to be driven by local changes in the ocean fluxes.

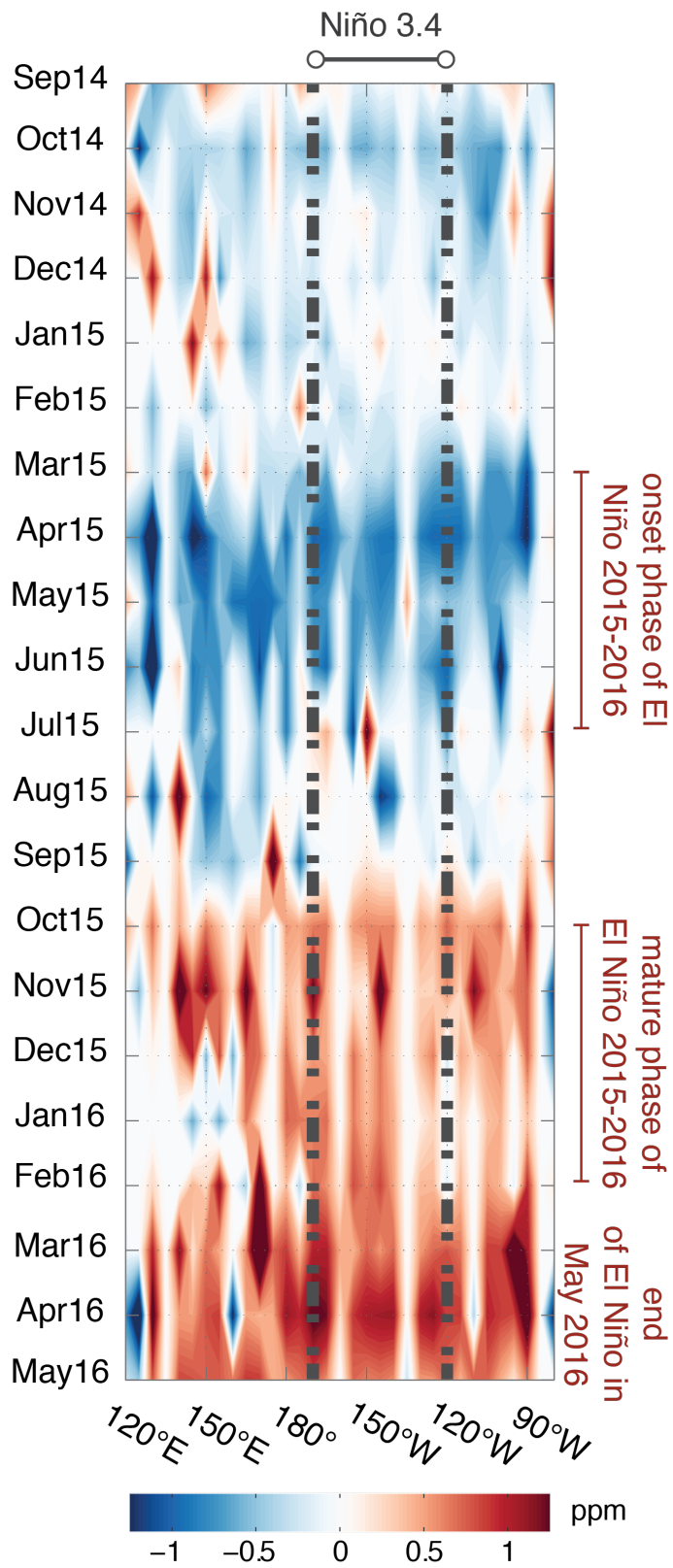


#### LEGEND

- Niño 3.4  $X_{CO_2}$  anom (minus) Global  $X_{CO_2}$  anom
- Niño 3.4  $X_{CO_2}$  anom (minus) trop. Atlantic  $X_{CO_2}$  anom
- ◆— Niño 3.4  $X_{CO_2}$  anom (minus) 20–30 N  $X_{CO_2}$  anom
- ◆— Niño 3.4  $X_{CO_2}$  anom (minus) 20–30 S  $X_{CO_2}$  anom



1 **Fig. 4.** Difference in  $X_{\text{CO}_2}$  anomalies between the Niño 3.4 region and (A) the globe, (B) the  
2 tropical Atlantic Ocean, (C) the subtropical Pacific Ocean from September 2014 to May 2016.  
3 Definitions of the regions are provided in Fig. 3. In Panel (A), we see a robust pattern of negative  
4  $X_{\text{CO}_2}$  anomaly between Niño 3.4 and the globe that is largest in 2015 and well synchronized with  
5 the onset phase of El Niño. In Panels (B) and (C), non-zero differences between Niño 3.4 and the  
6 other ocean basins indicate that the Niño 3.4 trend is not reproducible in other ocean basins; thus,  
7 allowing us to attribute the negative anomaly in Fig. 2B to a reduction in local  $\text{CO}_2$  outgassing  
8 over the tropical Pacific Ocean.



1 **Fig. 5.** Time evolution of the  $X_{CO_2}$  anomalies (ppm) averaged over 5°S-5°N. The x-axis  
2 represents longitude and the y-axis shows the time progressing from top to bottom in months.  
3 The 2015-2016 El Niño event and its onset and mature phases are highlighted to show the  
4 distinct responses observed over the tropical Pacific Ocean. The grey dashed lines capture the  
5 boundaries of the Niño 3.4 region. During the onset phase (i.e., March – July 2015), perceptible  
6 gradients are observable from the far western Pacific to the central Pacific (consistent with the  
7 increasing flux from west to east) along with high variability in the  $X_{CO_2}$  anomalies in the central  
8 Pacific. We also notice that the  $X_{CO_2}$  anomalies are smaller over the eastern Pacific, which is  
9 consistent with surface seawater  $pCO_2$  data collected on the TAO buoys (92). The transition  
10 from the ocean to the terrestrial signal happens between July and October 2015. Towards the  
11 latter stages of the El Niño event (i.e., November 2015 and later), the terrestrial signal dominates  
12 the observed trends in  $X_{CO_2}$  likely masking any underlying ocean signal.

# Supplementary Materials for

Influence of El Niño on atmospheric CO<sub>2</sub> over the tropical Pacific Ocean: findings  
from NASA's Orbiting Carbon Observatory-2 (OCO-2) mission

A. Chatterjee, M. M. Gierach, A. J. Sutton, R. A. Feely, D. Crisp, A. Eldering, M. R. Gunson, C.  
W. O'Dell, B. B. Stephens, D. S. Schimel

\*Correspondence should be addressed to: [abhishek.chatterjee@nasa.gov](mailto:abhishek.chatterjee@nasa.gov)

## **This PDF file includes:**

- *Materials and Methods*
  - X<sub>CO2</sub> retrievals from OCO-2 and GOSAT-ACOS
  - Generation of X<sub>CO2</sub> anomalies
  - pCO<sub>2</sub> observations from the TAO array
  - CO observations from the MOPITT instrument
- *Supporting Text*
  - Section A – Calculation of sea-to-air fluxes from the TAO and the OCO-2 datasets
  - Section B - Analyzing the sensitivity of X<sub>CO2</sub> anomalies to the curve fitting procedure
  - Section C - Uncertainty analyses for the trend in X<sub>CO2</sub> anomalies
  - Section D – Cross-correlation between X<sub>CO2</sub> anomalies and SST anomalies
- *Figs. S1 to S8*
- *Tables S1*
- *References*

## Materials and Methods

### *X<sub>CO2</sub> retrievals from OCO-2 and GOSAT-ACOS*

OCO-2 is NASA's first dedicated satellite mission for measuring column average, atmospheric carbon dioxide (CO<sub>2</sub>) dry air mole fraction (X<sub>CO2</sub>) with the accuracy, resolution, and coverage needed for quantifying CO<sub>2</sub> fluxes (sources and sinks) on regional scales over the globe (69, 94-95). Over the sunlit hemisphere, the OCO-2 mission collects nearly one million soundings per day (24 soundings/second) at approximately 3km<sup>2</sup> nadir resolution. After cloud and aerosol screening, between 7 and 12% of these soundings yield full-column estimates of CO<sub>2</sub> on monthly timescales (96-97).

The OCO-2 observing strategy (nadir/glint modes) has been refined over the first two years of operations to improve the measurement coverage and yield, especially over the ocean. The initial observing strategy recorded only glint or nadir observations over the entire sunlit hemisphere for a complete, 16-day, ground-track repeat cycle, and then used the other observing mode in the next 16-day cycle. This approach provided adequate coverage of oceans and continents on monthly timescales. In July 2015, this observation strategy was modified to alternate between glint and nadir observations on alternate orbits to yield more continuous coverage of the entire sunlit hemisphere every day. In November 2015, the observation strategy was further optimized to always-collect glint data on orbits that were primarily over the ocean.

The X<sub>CO2</sub> retrievals used in this work are based on the version 7B (v7B) Level 2 algorithm. These data are freely available via the Goddard Earth Sciences Data and Information Services Center (GES-DISC) from the start of mission operation. OCO-2 results are also being cross-calibrated and cross-validated with measurements and data products from the Japanese Greenhouse gases Observing SATellite (GOSAT, nicknamed "Ibuki"), so that these two satellite

1 datasets can be combined to produce a uniform  $X_{CO_2}$  climate data record for use by the carbon  
2 cycle science community. The GOSAT  $X_{CO_2}$  retrievals used in this study have been generated by  
3 version 7.3 (v7.3) of the ACOS algorithm (GOSAT-ACOS, 98-99). Only the high (H) gain  
4 observations are retained from the GOSAT-ACOS dataset. These data are bias-corrected using  
5 the same predictors as those used for the OCO-2 v7B dataset.

6 The  $X_{CO_2}$  estimates have been validated against results from the Total Carbon Column  
7 Observing Network (TCCON) and other standards to assess their accuracy and correct regional  
8 scale biases (71, 100). After bias correction and data screening, the median residual bias between  
9 OCO-2 and TCCON  $X_{CO_2}$  estimates are less than 0.5 ppm while the root-mean-square (RMS)  
10 differences between the two estimates are typically less than 1.5 ppm (71). Direct validation of  
11 the OCO-2  $X_{CO_2}$  estimates against TCCON sites has only revealed biases beyond 2 ppm for  
12 some months at Wollongong, Australia (34°S), whereas Ascension Island (10°S in the Atlantic  
13 Ocean) has not revealed any noticeable biases. Since there are no TCCON stations in the tropical  
14 Pacific Ocean, we must infer the quality of the ocean data from these validation sites in other  
15 ocean basins. The OCO-2 team has also noticed errors in the data over the Southern Hemisphere  
16 ocean that have a seasonal dependency. Those data are screened out using an airmass-dependent  
17 filter (70). Because the evaluation of systematic errors in these satellite retrievals is currently the  
18 subject of active research, we have carried out additional sensitivity tests (Section C) to ensure  
19 that these errors do not impact the findings in this study.

20 Typically, the  $X_{CO_2}$  retrievals are only performed on scenes nearly devoid of cloud and/or  
21 optically thick aerosol. Because of this, ENSO-induced changes in cloud patterns may cause  
22 slight changes in the locations of OCO-2 measurements, but are not expected to induce  
23 additional biases in these measurements. We find that the retrieval algorithm sees enough clear-

1 sky scenes to consistently generate an adequate number of high-quality soundings for the entire  
2 time period of this study. For a typical month (e.g., August 2015), we find that GOSAT-ACOS  
3 returns ~10K “good-quality” soundings while OCO-2 returns ~150K “good-quality” soundings  
4 globally. For OCO-2, 60% of the retrieved soundings are ocean glint observations. Thus, in  
5 August 2015, the total number of ocean glint soundings is ~96K. Both of these space-based  
6 missions provide significantly more coverage over the tropical Pacific Ocean relative to the  
7 sparse *in situ* monitoring network (Fig. S1). In fact, it is the continuous coverage from GOSAT  
8 and OCO-2 that allows us to generate a time series of  $X_{CO_2}$  over the tropical Pacific Ocean (Fig.  
9 S2) – for each month between June 2009 – May 2016 individual good-quality ocean glint  
10 soundings over the entire Niño 3.4 region are aggregated to generate a single monthly  $X_{CO_2}$   
11 estimate over Niño 3.4.

## 1 Generation of $X_{CO_2}$ anomalies

2           The time-series of  $X_{CO_2}$  (and in general, time-series of atmospheric  $CO_2$  concentrations)  
3 exhibit both a linear trend and a cyclo-stationary component due to the seasonal cycle (Fig. S2).  
4 To account for the seasonality and the upward trend of  $CO_2$ , we have adopted a two-step  
5 approach: (1) for each month, all  $X_{CO_2}$  retrievals from GOSAT-ACOS and OCO-2 are averaged  
6 over pre-specified domains (e.g., Niño 3.4, tropical Pacific Ocean, tropical Atlantic Ocean,  
7 global) assuming no temporal correlation between months, and (2) for an individual month, say  
8 August, we find a linear trend that best fits the  $X_{CO_2}$  data from 7-years of GOSAT-ACOS and  
9 OCO-2 observational record for that month, i.e., find the linear trend for August 2009, August  
10 2010, August 2011, August 2012, August 2013, August 2014, August 2015. Residuals from this  
11 linear trend (Fig. S3) are the  $X_{CO_2}$  anomalies that will be analyzed. Note that the first derivative  
12 of the trend (slope of the linear regression line) provides an estimate of the monthly  $X_{CO_2}$  growth  
13 rate. Simply comparing the growth rate values with those reported in previous studies delivers a  
14 necessary (but not sufficient) sanity check of our methodological framework. We have also  
15 explored the sensitivity of our calculated anomalies with respect to existing fitting methods  
16 (Section B, Fig. S5) and did not see any significant impact on our findings.

17           Mathematically, if  $e_{mo,yr}$  represents the monthly  $X_{CO_2}$  anomalies for a given year, then  
18 these are derived from Equation S1:

$$e_{mo,yr} = y_{mo,yr} - \hat{y}_{mo,yr} = y_{mo,yr} - (\alpha_{mo} + \beta_{mo}x_{yr}) \quad \dots \text{Equation S1}$$

19 where,  $y_{mo,yr}$  = observed monthly  $X_{CO_2}$  value for a given year,  $x_{yr} = 1, \dots, 7$  for the 7 years, and  
20  $\alpha$  and  $\beta$  are the intercept and slope parameters that are estimated during the linear regression  
21 procedure. From a physical standpoint,  $\beta_{mo}$  represents the monthly  $X_{CO_2}$  growth rate ( $\text{ppm yr}^{-1}$ )  
22 and  $\alpha_{mo}$  represents the monthly  $X_{CO_2}$  offset (ppm) relative to the start of our analyses period in



2009. This approach provides the flexibility of calculating the linear trend over any spatial domain – for example, globally, or over the entire tropical Pacific Ocean or separately for individual Niño regions. On monthly timescales, we do find slight differences in growth rates between the entire tropical Pacific Ocean and individual Niño regions – typically these differences are on the order of 0.01-0.2 ppm yr<sup>-1</sup>. On average the global growth rates vary between 1.88-2.37 ppm yr<sup>-1</sup> depending on the season. These numbers are consistent with previous studies (101-102) that have attempted to derive space-based X<sub>CO2</sub> growth rate over various spatial domains (e.g., global vs. Northern Hemisphere vs. Southern Hemisphere).

Due to the short time series of the OCO-2 record, we had to rely on the GOSAT-ACOS dataset to provide a climatological reference. While care was taken to use X<sub>CO2</sub> that are based on the same retrieval algorithm (OCO-2 v7B and GOSAT-ACOS v7.3), we recognize that stitching together data from two different instruments, i.e., GOSAT- and OCO-2 involves an implicit change in sampling strategy plus changes in observational density. Within the atmospheric trace gas remote-sensing community, this is a strategy that has been employed for generating climatologies from data available over a limited timespan – a typical example being the generation of ozone climatology using profile data from ozonesondes, observations from multiple satellite instruments, etc. (103-105). Section C discusses the sensitivity tests we have carried out to confirm that the derived X<sub>CO2</sub> anomalies are not being impacted due to this ‘*change of instrument*’ issue. In the future, as the OCO-2 data record grows, we will be able to revise the climatology based on a homogenous X<sub>CO2</sub> record, either from actual OCO-2 data or quasi-operational Level-3 maps (106) that will be made available as part of the OCO-2 product suite.

1 *pCO<sub>2</sub> observations from the TAO array*

2       The TAO (Tropical Atmosphere Ocean) array of moored buoys in the tropical Pacific  
3 Ocean provides real-time, in situ meteorological and oceanographic measurements (72).  
4 Atmospheric and surface seawater partial pressure of CO<sub>2</sub> (*p*CO<sub>2</sub>) is currently measured by  
5 Moored Autonomous *p*CO<sub>2</sub> (MAPCO<sub>2</sub>) systems maintained on the TAO array at 0°, 110°W; 0°,  
6 125°W; 0°, 140°W; 0°, 155°W; 0°, 170°W; 0°, 165°E; and 8°S, 165°E (38).

7       In brief, the MAPCO<sub>2</sub> system (39) utilizes an automated equilibrator-based gas collection  
8 system to measure surface seawater *x*CO<sub>2</sub> (the mole fraction of CO<sub>2</sub> in air in equilibrium with  
9 surface seawater) at approximately 14 cm depth and atmospheric *x*CO<sub>2</sub> at approximately 1.5 m  
10 above the sea surface every 3 hours. This *x*CO<sub>2</sub> (wet) measurement is made by a non-dispersive  
11 infrared gas analyzer (LI-820, LI-COR) calibrated before, during, and after field deployment  
12 with reference gases traceable to World Meteorological Organization standards prepared by  
13 NOAA's Earth System Research Laboratory. The MAPCO<sub>2</sub> system also measures sample  
14 temperature, pressure, and relative humidity to calculate *x*CO<sub>2</sub> (dry) based on the equations in  
15 (107). Sea surface temperature (SST) and salinity from TAO temperature and conductivity  
16 sensors are then used to calculate *p*CO<sub>2</sub> consistent with ocean carbon standard operating  
17 procedures as described in (39).

18       Once data are recovered from the field and quality controlled, 3-hourly CO<sub>2</sub> observations  
19 are archived at the Carbon Dioxide Information Analysis Center  
20 (<http://cdiac.ornl.gov/oceans/Moorings/>) and the National Centers for Environmental  
21 Information (<https://www.ncei.noaa.gov/>). Monthly averaged real-time observations of Δ*p*CO<sub>2</sub>  
22 (seawater *p*CO<sub>2</sub> – atmospheric *p*CO<sub>2</sub>) from September 2014 – May 2016 are shown in Fig. 2C  
23 and Table S1. Quality control checks on the *p*CO<sub>2</sub> observations reveal good measurements were

collected during this time period. Based on laboratory tests at NOAA Pacific Marine Environment Laboratory (PMEL) and field intercomparisons, estimates of uncertainty for quality-controlled air and seawater  $p\text{CO}_2$  measurements are  $\leq 2 \mu\text{atm}$  (39); however, uncertainty of preliminary monthly-averaged data are likely slightly higher ( $\leq 5 \mu\text{atm}$ ). Data plots from all TAO  $p\text{CO}_2$  locations, which include both real time and finalized data, are available at - [www.pmel.noaa.gov/co2/story/Open+Ocean+Moorings](http://www.pmel.noaa.gov/co2/story/Open+Ocean+Moorings).

Figure 2C captures the temporal trend in the  $\Delta p\text{CO}_2$  values from the  $0^\circ$ ,  $170^\circ\text{W}$  TAO array buoy, which is located in the western-most portion of the Niño 3.4 region. Preliminary analyses seem to suggest that this buoy registered the first response to the onset of El Niño conditions. On the other hand, observations at  $0^\circ$ ,  $110^\circ\text{W}$  from the TAO array buoy (<https://www.pmel.noaa.gov/co2/story/Open+Ocean+Moorings>) seem to indicate that upwelling of high dissolved inorganic carbon (DIC) water continued in the central and eastern-most portion of the Niño 3.4 region till early Fall 2015 with only brief periods (November 2015 – February 2016) where surface seawater  $p\text{CO}_2$  was close to equilibrium with atmospheric values. Observations from these more eastern sites indicate diverse regimes operating across the tropical Pacific; Fig. 5 qualitatively demonstrates that the  $X_{\text{CO}_2}$  anomalies capture these regional gradients depending on its magnitude, seasonality, location, etc. As more *in situ* measurements become available, quantitative investigations are ongoing to check how well the OCO-2 observations can resolve such regional gradients.

## CO observations from the MOPITT instrument

Since March 2000, the MOPITT instrument on board the NASA/EOS Terra platform has been monitoring the CO content in the troposphere. Details about the retrieval algorithm, its validation and uncertainties are provided in Deeter *et al.* (108, 112-113) and Emmons *et al.* (109) while analyses and discussion of decadal CO trends are provided in more recent studies (110-111). An instrument cooler failure between May and August 2001 significantly impacted the retrieval mean levels before and after the instrument anomaly. Hence for the sake of homogeneity, we select data during the period June 2002 - May 2016 for generating a climatological value of CO content in the atmosphere. Unlike the shorter X<sub>CO2</sub> record, the availability of a long and homogeneous CO data record (>14 years) from a single instrument makes the generation of the climatology (and associated anomaly calculations) straightforward. Based on the recommendation of the MOPITT team, we use the Level 3 MOPITTv6 CO (112) estimated from the thermal-infrared (TIR) channel. TIR measurements offer the best description of CO emissions from fires due to the large thermal contrast between the lower troposphere and free troposphere due to intense surface heating. For this study, we look at the CO Volume Mixing Ratio (VMR) for both the total column and at an individual atmospheric pressure level at 700 hPa.

Given that the two largest surface sources of CO are the combustion of fossil fuel and the combustion of biomass (forest and savanna fires, biofuel use, and waste burning), MOPITT CO anomalies have been used to track emission from fires, including El Niño-related ones (114-117). While the surface level anomalies can detect the onset of fires immediately (i.e., without any time lag), CO anomalies at higher levels in the atmosphere increase gradually and exhibit significantly smaller peak anomaly values than the surface. These features are consistent with the

1 expected lag and dilution associated with vertical mixing. Fig. S4 shows that the impact of fire  
2 emissions between August and October 2015 from S.E. Asia/Indonesia are clearly visible over  
3 the tropical Pacific Ocean. The largest anomalous sources of CO occur over the Indonesian  
4 regions, which are emitted as strong pulses over the 3-month window. These maps also rule out  
5 biomass burning emissions from other regions, such as Africa and South America that can  
6 potentially influence the rise in CO and CO<sub>2</sub> concentrations over our region of interest (i.e., Niño  
7 3.4).

8       Because the signal from enhanced fire emissions are correlated with drought, however,  
9 we cannot quantitatively discriminate the relative roles of reduction in biospheric uptake due to  
10 warmer, drier climates or emissions from biomass burning by just looking at the trends in the  
11 anomalies in the CO<sub>2</sub> and the CO data. What we can discern is the timing of the large tropical  
12 source (of which the biomass burning emissions are a major contributor) and its impact on the  
13 rise in CO<sub>2</sub> concentration anomalies from August 2015 onwards.

## 1 **Supporting Text**

### 2 Section A: Calculation of sea-to-air fluxes from the TAO and the OCO-2 datasets

#### 3 **Calculation of sea-to-air flux from $p\text{CO}_2$ observations**

4 Following Wanninkhof (118), the net flux of  $\text{CO}_2$  across the air-sea interface,  $\mathbf{F}$  (mass  
5  $\text{area}^{-1} \text{ time}^{-1}$ ) is calculated as the product of the gas transfer velocity  $\mathbf{k}$  ( $\text{length time}^{-1}$ ), the  
6 solubility of  $\text{CO}_2$ ,  $\mathbf{s}$  ( $\text{mass volume}^{-1} \text{ pressure}^{-1}$ ), and the  $p\text{CO}_2$  (pressure) difference between the  
7 ocean and atmosphere ( $p\text{CO}_2^{\text{sw}} - p\text{CO}_2^{\text{atm}}$ ), according to Equations S2 and S3:

$$\mathbf{F} = \mathbf{k}\mathbf{s}(p\text{CO}_2^{\text{sw}} - p\text{CO}_2^{\text{atm}}) \quad \dots \text{Equation S2}$$

$$\mathbf{k} = 0.251\mathbf{U}_{10}^2(\mathbf{S}_c/660)^{-0.5} \quad \dots \text{Equation S3}$$

8 where,  $\mathbf{S}_c$  is the Schmidt number for  $\text{CO}_2$ , and  $\mathbf{U}_{10}$  is the wind speed at 10m height. By  
9 convention, the units of  $\mathbf{k}$  are in  $\text{cm h}^{-1}$ ,  $\mathbf{U}_{10}$  is in  $\text{m s}^{-1}$  and units of the coefficient 0.251 are ( $\text{cm}$   
10  $\text{h}^{-1}$ ) ( $\text{m s}^{-1}$ ) $^{-2}$ . Daily averaged wind speeds were acquired from the Modern-Era Retrospective  
11 analysis for Research and Applications, Version 2, or MERRA-2 (119).

12 Based on these equations, the calculated fluxes at TAO  $0^\circ$ ,  $170^\circ\text{W}$  are  $0.21 \pm 0.20$  ( $1\sigma$ )  
13  $\text{gC m}^{-2} \text{ month}^{-1}$  between April 2015 – March 2016 (i.e., during the El Niño 2015-2016 event).  
14 This is a flux reduction of 84% relative to the neutral April 2014 – March 2015 period during  
15 which the magnitude of flux was  $1.35 \pm 0.20$  ( $1\sigma$ )  $\text{gC m}^{-2} \text{ month}^{-1}$ . Note that this flux difference  
16 is only representative of the western-most portion of the Niño 3.4 region. The  $\text{CO}_2$  fluxes and the  
17 magnitude of flux reduction could be considerably different in the eastern-most portions of the  
18 tropical Pacific Ocean. Studies reporting on the magnitude of air-sea flux reduction across the  
19 tropical Pacific Ocean during El Niño events typically report a flux reduction of ~40-60%.

20

## 1 Calculation of sea-to-air flux from $X_{CO_2}$ observations

2 Following Gurney *et al.* (120), we have used simple atmospheric transport model  
3 simulations to assess whether the magnitude of ocean flux anomaly based on the  $pCO_2$   
4 observations is consistent with the anomaly observed in the  $X_{CO_2}$  estimates. For the 16 models  
5 participating in the TransCom3 Level 1 experiment (T3L1) (121), we have calculated the  
6 average column mean  $CO_2$  enhancement over the Niño 3.4 region for the Eastern Equatorial  
7 Pacific basis function (region 14) fluxes. As per the TransCom experiment protocol, the fluxes  
8 for this basis function was set to a constant  $1 \text{ PgC yr}^{-1}$  evenly distributed within the region. These  
9 data are precomputed and available as part of the TransCom 3 experiments at -  
10 [http://transcom.project.asu.edu/transcom03\\_output.php](http://transcom.project.asu.edu/transcom03_output.php). The average difference between Niño  
11 3.4 region and a global reference column mean is  $0.43 \pm 0.09 (1\sigma)$  ppm. The global reference is  
12 based on a latitudinal cutoff of  $60^\circ\text{S}$ - $60^\circ\text{N}$  keeping in mind the range of latitudes over which  
13 OCO-2 observations are available. Since the basis function used in these experiments was  $1 \text{ PgC}$   
14  $\text{yr}^{-1}$  constant emission, this gives a sensitivity of  $1/0.43 = 2.33 \text{ PgC yr}^{-1}$  per ppm, or for a  $0.26 \pm$   
15  $0.09 (1\sigma)$  ppm dip (as seen from Fig. 4A over May, June, July, August 2015) about  $0.60 \pm 0.21$   
16  $(1\sigma) \text{ PgC yr}^{-1}$ . Given that the dip in  $X_{CO_2}$  anomalies are observed over a period 4 months long  
17 (Fig. 4A), this would suggest a total flux of  $0.20 \pm 0.07 (1\sigma) \text{ PgC}$ . As per the TransCom  
18 framework, note that this is an implied flux difference, in  $\text{PgC}$  absolute. Thus, if the original  
19 magnitude of sea-to-air flux is  $0.5 \text{ PgC yr}^{-1}$  (36), then the implied reduction in the flux  
20 outgassing is  $0.2/0.5 * 100 = 40 \pm 14 (1\sigma) \%$  (i.e., 26-54%). This simple but effective calculation  
21 provides a necessary sanity check on the magnitude of the signal observed from the  $X_{CO_2}$  data.

22 In reality, the changes in the surface fluxes are far more complicated with processes  
23 occurring at distinct spatiotemporal scales and with different levels of maturity. The simple

1 analysis presented here does not take into account spatial gradients in fluxes within the east  
2 equatorial Pacific region itself or between the east and west tropical Pacific Ocean, all of which  
3 may have been possible for the 2015-2016 El Niño event. More detailed analyses using  
4 atmospheric inverse modeling/data assimilation techniques and both satellite and *in situ* data are  
5 necessary (and ongoing) to parse out the grid-scale air-sea flux magnitudes over the tropical  
6 Pacific Ocean.



1 Section B: Analyzing the sensitivity of  $X_{CO_2}$  anomalies to the curve fitting procedure

2       Pickers and Manning (122) discuss that significant bias and uncertainty can be introduced  
3 in the application of curve fitting programs to atmospheric time series. The specific curve fitting  
4 method used in this study was designed keeping in mind the attributes of atmospheric CO<sub>2</sub>  
5 concentrations (i.e., both long-term growth rate and seasonal cycle). In principle, the overall  
6 framework is analogous to the one currently used at NOAA ('CCGCRV') to fit observation time  
7 series from the NOAA *in situ* network. Originally based on Thoning *et al.* (123), the CCGCRV  
8 curve fitting method represents the long-term growth rate by a polynomial function, the annual  
9 oscillation by harmonics of a yearly cycle and then uses a low pass filter to retain interannual and  
10 short term variations in the fitted curve. There is no set rule on the number of polynomial terms  
11 in the function, and it depends on the application and user preference.

12       We have used the CCGCRV curve fitting method to detrend our  $X_{CO_2}$  time series, and re-  
13 calculated the anomalies and the growth rates (Fig. S5). A simple linear term was used for the  
14 polynomial part of the function to make the overall function as comparable as possible to our  
15 curve fitting method. We find that the overall pattern in the  $X_{CO_2}$  anomalies (negative anomaly  
16 during Summer 2015 followed by a positive anomaly in Fall 2015) is consistent for both  
17 methods. This implies that the curve fitting procedure did not introduce any spurious bias or  
18 trend onto our analyses.

### Section C: Uncertainty analyses for the trend in $X_{CO_2}$ anomalies

An ensemble approach is used to quantify the error associated with the time series of the Niño 3.4  $X_{CO_2}$  anomaly. Fig. S6 shows specific tracks that GOSAT flies over, and only 6 of those tracks lie within the Niño 3.4 region. We create an ensemble of small regions that are roughly 200 km x 400 km around those individual GOSAT tracks. For each of these regions (30 in total), we apply the same methodology to generate the  $X_{CO_2}$  climatology and extract the associated anomaly for our study time period (September 2014 – May 2016). The resultant spread among the 30 ensemble members defines the  $1\sigma$  standard deviation for the mean  $X_{CO_2}$  anomaly line (Fig. 2B), which is still derived from the full Niño 3.4 region.

We have carried out an additional sensitivity test (Fig. S7) where we have systematically added/subtracted constant mean bias values (0.1-1ppm) to the ocean glint retrievals used in this study. Given the lack of validation data over the tropical Pacific Ocean, it is necessary to ascertain that residual systematic errors in the ocean glint retrievals (71, 100) do not alias onto our calculations. Fig. S7 illustrates that even in the worst-case scenario, where the ocean glint retrievals have a low bias (i.e., negative) of 1 ppm, the overall temporal structure of the  $X_{CO_2}$  anomaly is conserved. The impact on the  $X_{CO_2}$  anomaly line is that it shifts up or down depending on the magnitude of the bias, which in turn impacts the inference of the magnitude of the air-sea fluxes. Certainly, a more complicated structure of the residual biases (e.g., coherent spatial and temporal dependency or correlations between biases) will impact these trends in a different manner. But based on our current understanding of the satellite retrievals, these sensitivity tests and the ocean basin-related diagnostics (Figs. 3 and 4) show that the findings are robust to a couple of first order caveats that have not been resolved for the global OCO-2 dataset as a whole.

#### Section D: Cross-correlation between $X_{CO_2}$ anomalies and SST anomalies

We have investigated the cross-correlation between the  $X_{CO_2}$  anomalies and the ONI index (which are derived from the Niño 3.4 SST anomalies) for the entire period of June 2009 – May 2016 ( $n=84$ ) to test the magnitude and phase of the relationship between the two variables. The largest correlations are found for  $X_{CO_2}$  anomalies lagging the ONI by 1-2 months (Fig. S8). These correlations are significant at the 95% level based on the random phase test of Ebisuzaki (124). Previous studies (6, 13, 14, 31) have looked at carbon cycle related anomalies (i.e., anomalies in  $CO_2$  concentrations or  $CO_2$  fluxes) and tested its phasing and strength with a suite of ENSO indices (e.g., SOI, Niño 3 SST anomalies, etc.). Jones *et al.* (14) provides the closest analogy to this work, where they reported a lag of 3 months between the  $CO_2$  concentrations measured at Mauna Loa and Niño 3 (5°S-5°N, 90°W-150°W) SST anomalies.

We believe that the longer response time of the Mauna Loa  $CO_2$  anomalies to SST anomalies is not necessarily a feature of the carbon cycle but rather due to a time lag associated between the driver (SST) and the response ( $CO_2$ ) measured at a location far away from the center of action. The availability of  $X_{CO_2}$  retrievals directly over the region of action (tropical Pacific Ocean and the Niño 3.4 region) provides a new tool for understanding both the strength of correlation of atmospheric  $CO_2$  changes with ENSO and the real-time lag associated with the ocean carbon cycle response.

## Supporting Figures and Tables

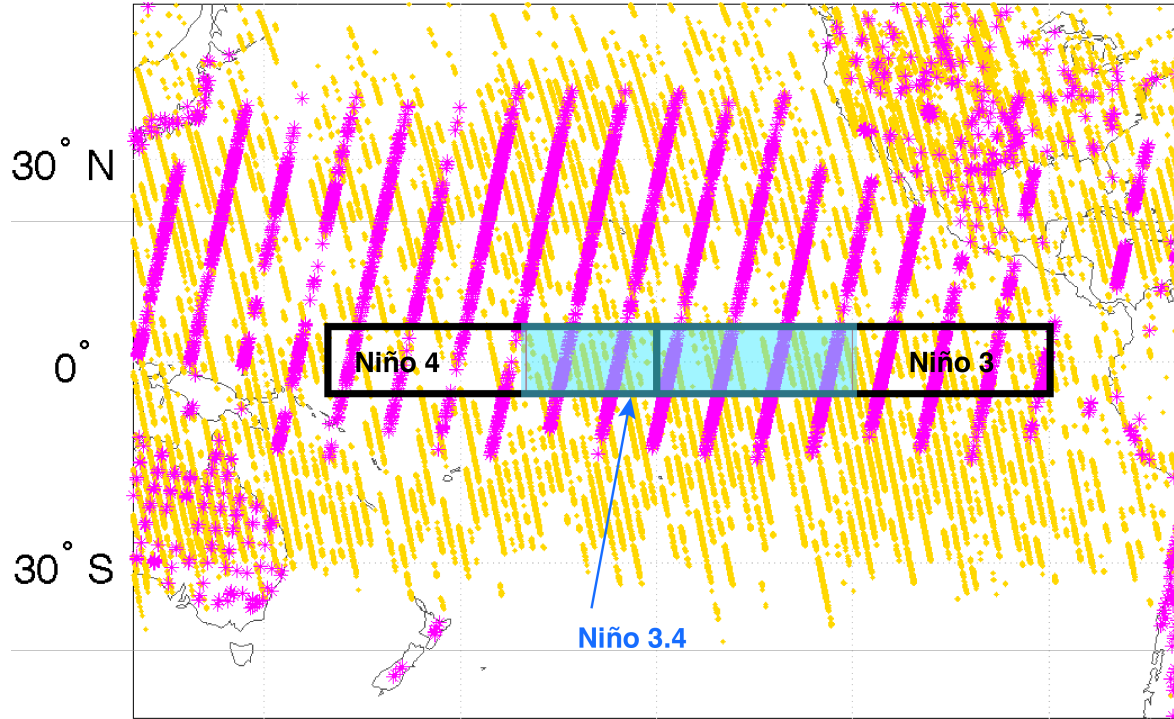


**Fig. S1.** Coverage over the Pacific Ocean from GOSAT-ACOS v7.3 (magenta) and OCO-2 v7B (gold) for one representative month in 2015. Relative to GOSAT, OCO-2 provides more observations over the open ocean (~100x more soundings per day) with higher accuracy and precision. Also shown are the Niño regions over the tropical Pacific Ocean that are traditionally used to study and define El Niño events.

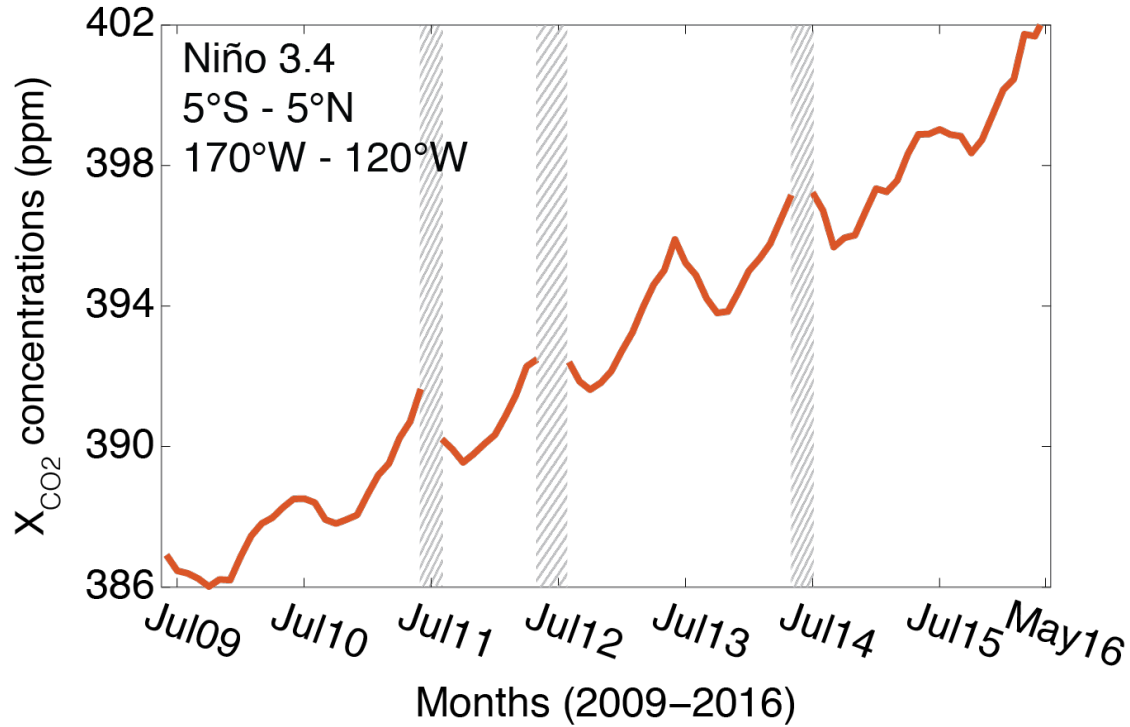


**Fig. S2.** Time-series of X<sub>CO2</sub> over the Niño 3.4 region for seven years (June 2009 – May 2016) after combining the GOSAT and the OCO-2 data streams. The availability of space-based observations over remote locations, such as the Niño 3.4 region, allows us to stitch together a long-time series of X<sub>CO2</sub> concentrations from which the X<sub>CO2</sub> anomalies can be deduced (Fig. S3). Grey-hatched portions indicate time-periods during which data is not available over the Niño 3.4 region (July 2011, June 2012 – July 2012 and June 2014)– either due to instrument downtime or planned maintenance.

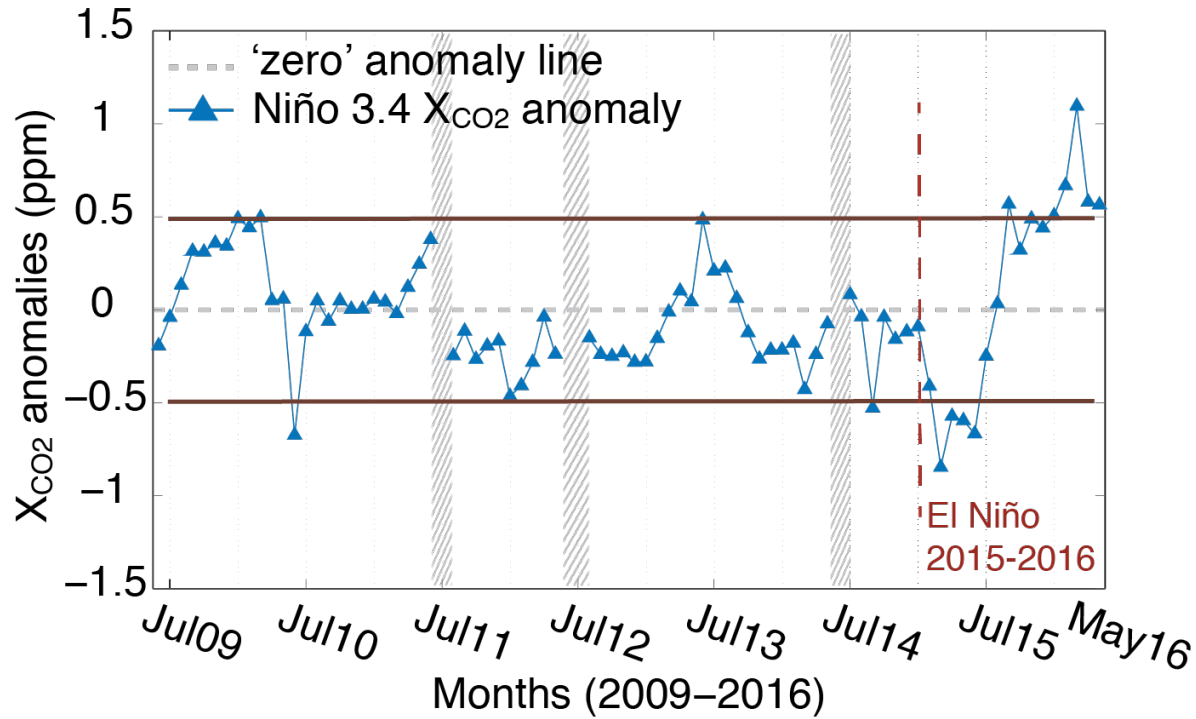


**Fig. S3.** Multi-year time series of  $X_{CO_2}$  anomalies over the Niño 3.4 region. The timespan covers June 2009 to May 2016. Grey-hatched portions indicate time-periods during which data is not available over the Niño 3.4 region (July 2011, June 2012 – July 2012 and June 2014)– either due to instrument downtime or planned maintenance. The horizontal brown lines indicate the range of uncertainty ( $\pm 0.5$  ppm) expected in the  $X_{CO_2}$  data. The vertical dashed red line shows the time period from which a subset of this time series (September 2014 to May 2016) has been explored in detail in this study. Comparison to previous years illustrates, however, that the anomaly signature observed during the 2015-2016 period are distinct relative to other periods.

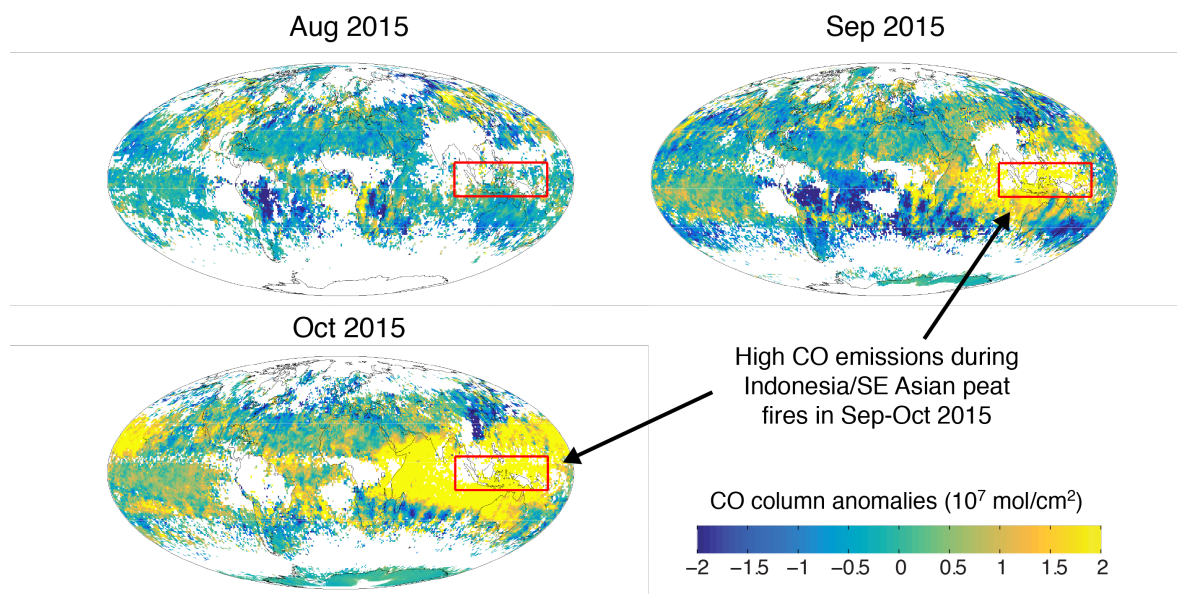


**Fig. S4.** Spatial distribution of CO total column anomalies retrieved from the MOPITT instrument between August and October 2015. The red rectangle shows the location of SE Asia and Indonesia. Note the spike in CO anomalies during September 2015 due to the Indonesian peat fires, and subsequent advection (visible as a yellow blob) eastward across the tropical Pacific Ocean and westward over the tropical Indian Ocean. The peak values of CO anomalies occur during October 2015, which is also evident from the time series in Fig. 2D.

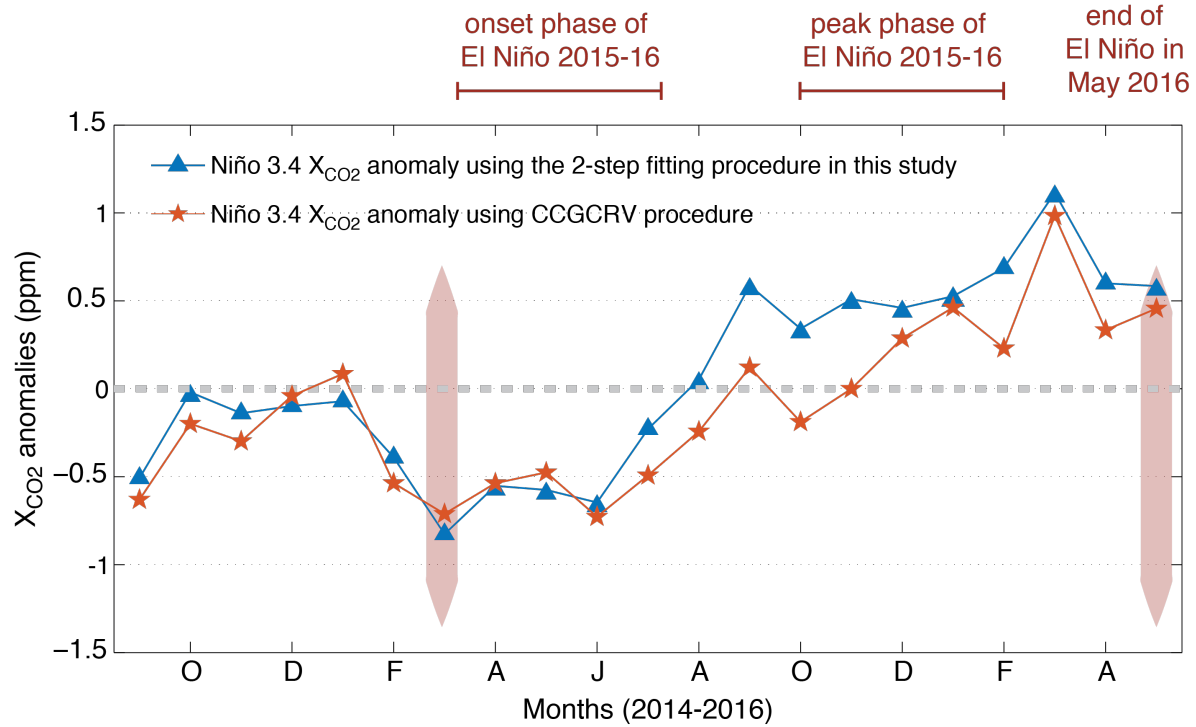


**Fig. S5.** Time series of  $X_{CO_2}$  anomalies generated by two different curve-fitting methods – the procedure used in this study (blue line with diamonds) and the traditional ‘CCGCRV’ procedure (orange line with stars). Both methods generate similar trends in the anomaly during the onset phase (i.e., negative anomaly in  $X_{CO_2}$ ) and the mature phase of El Niño (i.e., steep increase in  $X_{CO_2}$  anomaly). However, we do note a systematic difference in the magnitude of the positive  $X_{CO_2}$  anomaly (August – December 2015) likely due to the difference in the number of parameters used in the two curve-fitting procedures.



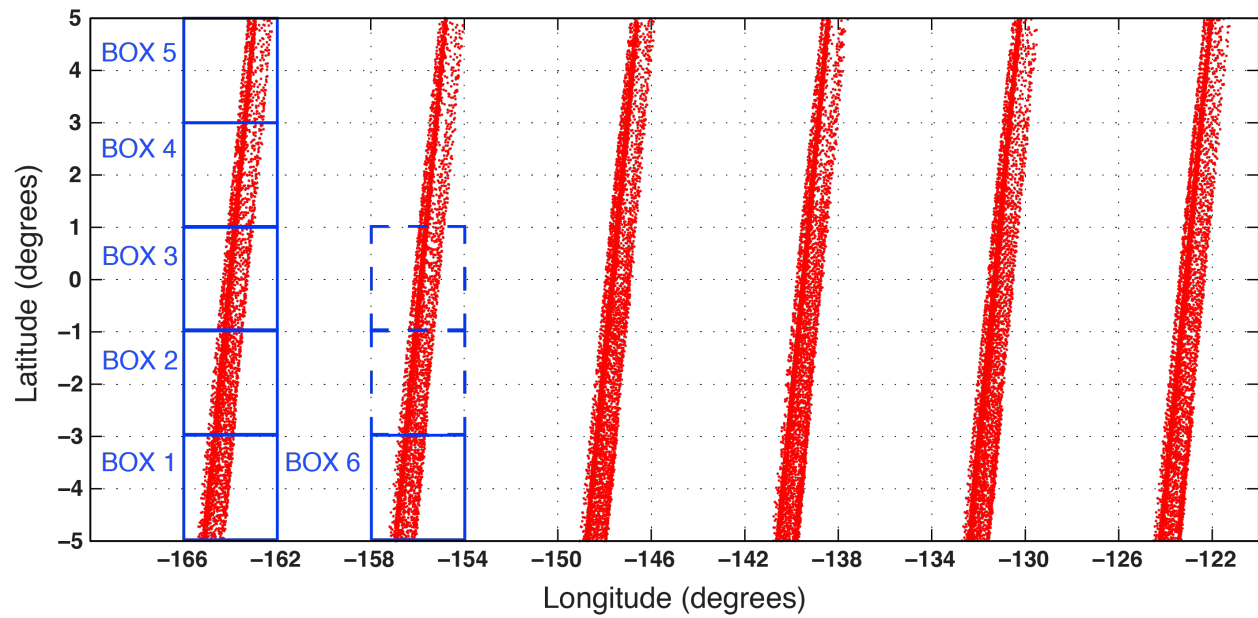


**Fig. S6.** Schematic of the methodology used to generate an ensemble of boxes within the Niño 3.4 domain. Each individual box is centered around a GOSAT track – this ensures that the spatial coverage provided by the two remote sensing missions (GOSAT and OCO-2) are roughly equivalent within the box, thus minimizing the impact of differences in sampling density between the two instruments.

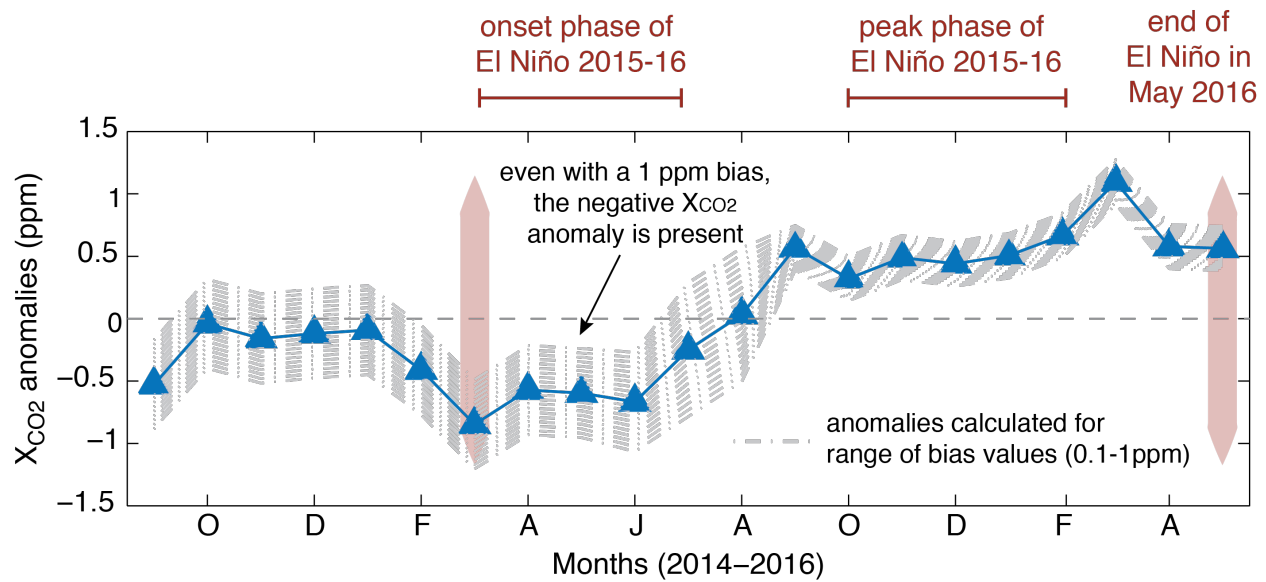
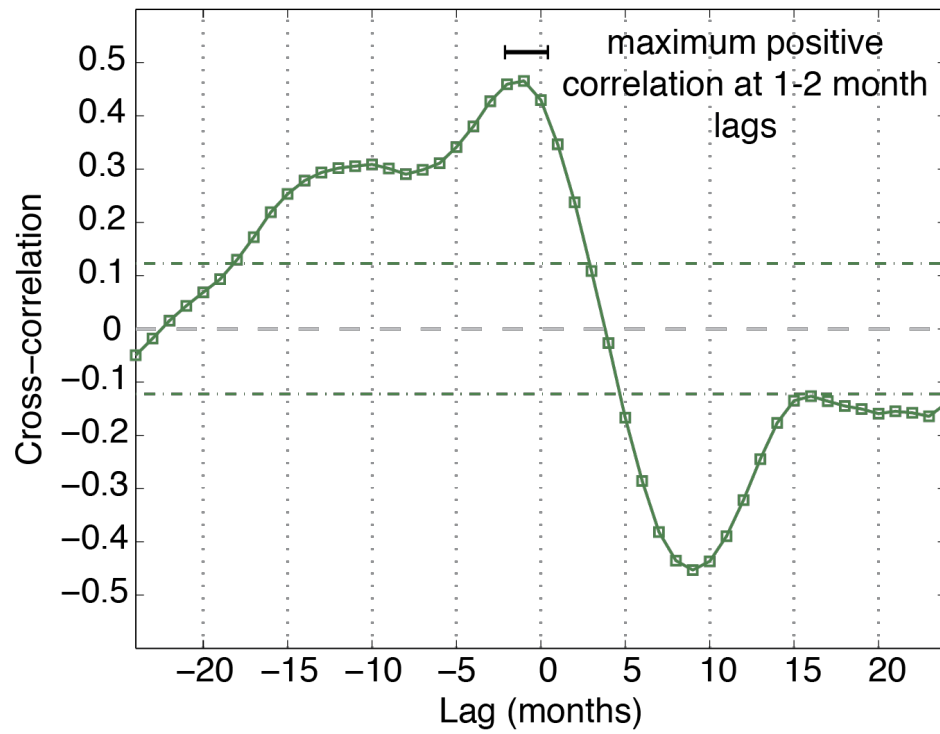


**Fig. S7.** Uncertainty associated with the  $X_{CO_2}$  anomaly time series given residual systematic errors in the ocean glint retrievals. A range of constant mean bias values from  $\pm 0.1$  to  $\pm 1.0$  ppm were added to the ocean glint retrievals from OCO-2, and the  $X_{CO_2}$  anomaly re-calculated for each bias level. Even in the worst-case scenario (low 1 ppm bias over the tropical Pacific Ocean), the overall temporal structure of the ocean and the terrestrial responses are conserved. The magnitude of the  $X_{CO_2}$  anomaly shifts upward or downward, which will have consequences for the inferred changes in ocean/land –atmosphere fluxes.



1  
2 **Fig. S8.** Lag correlation of ONI against monthly  $X_{CO2}$  anomalies in the Niño 3.4 region. Lags  
3 less than 0 indicate a delay in the response of the  $X_{CO2}$  anomalies to the SST anomalies. The  
4 horizontal dashed green lines are based on a non-parametric test and indicate the correlation  
5 required to meet the 95% significance criteria.

1

Month	Year	Pressure (hPa)	sw $x\text{CO}_2$ ( $\mu\text{mol mol}^{-1}$ )	air $x\text{CO}_2$ ( $\mu\text{mol mol}^{-1}$ )	SST ( $^{\circ}\text{C}$ )	SSS (psu)	$\Delta p\text{CO}_2$ ( $\mu\text{atm}$ )
10	2014	1008.4	475.0	397.5	28.42	35.31	74.3
11	2014	1007.1	471.5	397.1	28.91	35.08	71.1
12	2014	1005.7	469.3	397.5	29.12	34.72	68.5
1	2015	1005.9	480.2	398.1	28.68	35.15	78.4
2	2015	1006.5	483.0	397.9	28.50	35.18	81.3
3	2015	1006.5	470.0	398.1	28.97	35.15	68.6
4	2015	1006.7	458.6	397.1	29.59	35.07	58.7
5	2015	1007.4	431.5	396.7	29.93	34.82	33.2
6	2015	1006.1	409.8	396.7	30.18	34.54	12.5
7	2015	1007.8	407.3	396.7	30.02	34.44	10.1
8	2015	1007.1	402.6	396.5	30.36	34.38	5.8
9	2015	1007.4	404.9	396.0	30.53	34.32	8.4
10	2015	1007.7	402.5	395.6	29.87	34.23	6.5
11	2015	1005.8	411.6	395.9	29.09	34.25	14.7
12	2015	1006.9	400.0	399.0	30.52	34.12	0.9
1	2016	1007.7	402.0	398.9	29.75	34.23	3.0
2	2016	1007.2	409.5	398.4	29.76	34.34	10.5
3	2016	1008.8	443.6	398.6	29.59	34.89	42.2
4	2016	1008.7	476.6	399.8	28.85	35.12	73.6
5	2016	1009.3	485.3	399.1	28.52	35.22	82.6

2

3 **Table S1.** Monthly-averaged real time data from the TAO 0°, 170°W mooring used to calculate4  $\Delta p\text{CO}_2$ . Monthly atmospheric pressure and seawater (sw) and air  $x\text{CO}_2$  values are averaged from5 3-hourly MAPCO<sub>2</sub> data. Monthly SST and SSS values are averaged from daily-averaged

6 National Data Buoy Center (NDBC) TAO CTD data (from:

7 [http://tao.ndbc.noaa.gov/tao/data\\_download/search\\_map.shtml](http://tao.ndbc.noaa.gov/tao/data_download/search_map.shtml)). Note that the October 2014

8 monthly average only includes data from 10/15/2014 - 10/31/2014; all other months include a

9 full month of data. Surface CTD or real time data transmissions seemed to intermittently fail at

10 this site between 11/16/2014 and 11/30/2015, and were replaced by data from the TAO 2°N,

11 170°W mooring (during data overlap in the time series, TAO 2°N, 170°W SST and SSS were -

12  $0.04 \pm 0.44$  ( $1\sigma$ ) and  $0.16 \pm 0.18$  ( $1\sigma$ ), respectively, compared to 0°, 170°W).

## Supporting References and Notes

94. D. Crisp *et al.*, The orbiting carbon observatory (OCO) mission. *Trace Constituents in the Troposphere and Lower Stratosphere* **34**, 700-709 (2004).
95. R. Pollock *et al.*, The Orbiting Carbon Observatory instrument: performance of the OCO instrument and plans for the OCO-2 instrument. *Proc. SPIE 7826, Sensors, Systems and Next Generation Satellites – XIV* **78260W** (2010).
96. T. E. Taylor *et al.*, Orbiting Carbon Observatory-2 (OCO-2) cloud screening algorithms: validation against collocated MODIS and CALIOP data. *Atmospheric Measurement Techniques* **9**, 973–989 (2016).
97. R. Nelson *et al.*, The potential of clear-sky carbon dioxide satellite retrievals. *Atmospheric Measurement Techniques* **9**, 1671–1684 (2016).
98. C. O'Dell *et al.*, The ACOS CO<sub>2</sub> retrieval algorithm – Part 1: Description and validation against synthetic observations. *Atmospheric Measurement Techniques* **5**, 99-121 (2012).
99. D. Crisp *et al.*, The ACOS CO<sub>2</sub> retrieval algorithm--Part II: Global X<sub>CO2</sub> data characterization. *Atmospheric Measurement Techniques* **5**, 687–707 (2012).
100. J. Worden *et al.*, Evaluation, Validation, And Attribution Of OCO-2 X<sub>CO2</sub> Uncertainties. *Atmos. Meas. Tech. Disc.* Available at doi:10.5194/amt-2016-175, in review (2016).
101. H. Lindqvist *et al.*, Does GOSAT capture the true seasonal cycle of carbon dioxide? *Atmospheric Chemistry and Physics* **15**, 13023–13040 (2015).
102. O. Schneising *et al.*, Long-term analysis of carbon dioxide and methane column-averaged mole fractions retrieved from SCIAMACHY. *Atmospheric Chemistry and*

- Physics* **11**, 2863–2880 (2011).
103. J. P. F. Fortuin, H. Kelder, An ozone climatology based on ozonesonde and satellite measurements. *Journal of Geophysical Research-Atmospheres* **103**, 31709 – 31734 (1998).
104. W. J. Randel, F. Wu, A stratospheric ozone profile data set for 1979–2005: Variability, trends, and comparisons with column ozone data. *Journal of Geophysical Research-Atmospheres* **112**, D06313 (2007).
105. R. D. McPeters, G. J. Labow, Climatology 2011: An MLS and sonde derived ozone climatology for satellite retrieval algorithms. *Journal of Geophysical Research-Atmospheres* **117**, D10303 (2012).
106. H. Nguyen, N. Cressie, A. Braverman, Multivariate Spatial Data Fusion for Very Large Remote Sensing Datasets. *Remote Sensing* **9**, 142 (2017).
107. R. F. Weiss, Carbon dioxide in water and seawater: the solubility of a non-ideal gas. *Marine Chemistry* **2**, 203–215 (1974).
108. M. N. Deeter *et al.*, Operational carbon monoxide retrieval algorithm and selected results for the MOPITT instrument. *Journal of Geophysical Research-Atmospheres* **108**, 4399 (2003).
109. L. Emmons *et al.*, Validation of Measurements of Pollution in the Troposphere (MOPITT) CO retrievals with aircraft in situ profiles. *Journal of Geophysical Research-Atmospheres* **109**, 13 (2004).
110. H. M. Worden *et al.*, Decadal record of satellite carbon monoxide observations. *Atmospheric Chemistry and Physics* **13**, 837-850 (2013).
111. Y. Yin *et al.*, Decadal trends in global CO emissions as seen by MOPITT.

- Atmospheric Chemistry and Physics* **15**, 13433-13451 (2015).
112. M. N. Deeter *et al.*, The MOPITT Version 6 product: algorithm enhancements and validation. *Atmospheric Measurement Techniques* **7**, 3623-3632 (2014).
113. M. N. Deeter *et al.*, Validation and analysis of MOPITT CO observations of the Amazon Basin. *Atmospheric Measurement Techniques* **9**, 3999-4012 (2016).
114. J. F. Lamarque *et al.*, Identification of CO plumes from MOPITT data: Application to the August 2000 Idaho-Montana forest fires. *Geophysical Research Letters* **30**, 1688 (2003).
115. A. Arellano *et al.*, Time-dependent inversion estimates of global biomass-burning CO emissions using Measurement of Pollution in the Troposphere (MOPITT) measurements. *Journal of Geophysical Research-Atmospheres* **111**, D09303 (2006).
116. Z. Jiang *et al.*, Impact of model errors in convective transport on CO source estimates inferred from MOPITT CO retrievals. *Journal of Geophysical Research-Atmospheres* **118**, 2073–2083 (2013).
117. J. Worden *et al.*, El Niño, the 2006 Indonesian peat fires, and the distribution of atmospheric methane. *Geophysical Research Letters* **40**, 4938-4943 (2013).
118. R. Wanninkhof, Relationship between the wind speed and gas exchange over the ocean revisited. *Limnology and Oceanography - Methods* **12**, 351-362 (2014).
119. M. G. Bosilovich *et al.*, “MERRA-2: File Specification” (Tech. Rep. Global Modeling and Assimilation Office, Office Note No. 9, 2016).
120. K. R. Gurney *et al.*, TransCom 3 CO<sub>2</sub> inversion intercomparison: 1. Annual mean control results and sensitivity to transport and prior flux information. *Tellus Series B-Chemical and Physical Meteorology* **55**, 555-579 (2003).

- 1        121.        K. R. Gurney *et al.*, Towards robust regional estimates of CO<sub>2</sub> sources and sinks using  
2                atmospheric transport models. *Nature* **415**, 626-630 (2002).
- 3        122.        P. A. Pickers, A. C. Manning, Investigating bias in the application of curve fitting  
4                programs to atmospheric time series. *Atmospheric Measurement Techniques* **8**, 1469-  
5                1489 (2015).
- 6        123.        K. W. Thoning, P. P. Tans, W. D. Komhyr, Atmospheric carbon dioxide at Mauna  
7                Loa Observatory, 2. Analysis of the NOAA/GMCC data, 1974-1985. *Journal of*  
8                *Geophysical Research-Atmospheres* **94**, 8549-8565 (1989).
- 9        124.        W. Ebisuzaki, A Method to Estimate the Statistical Significance of a Correlation  
10               When the Data Are Serially Correlated. *Journal of Climate* **10**, 2147-2153 (1997).